Optical depth to reionization in a universe with multiple inhomogeneous domains

Shashank Shekhar Pandey,[1,*] Ruchika,[2,3,4,†] Subhadeep Mukherjee,[1,‡] and A. S. Majumdar[1,§]

[1]*Department of Astrophysics and High Energy Physics, S. N. Bose National Centre for Basic Sciences, JD Block, Sector III, Salt Lake City, Kolkata-700106, India*

[2]*Departamento de Física Fundamental and IUFFyM, Universidad de Salamanca, E-37008 Salamanca, Spain*

[3]*INFN, Sezione di Roma, Piazzale Aldo Moro 2, I-00185 Roma, Italy*

[4]*Dipartimento di Fisica, Università di Roma "La Sapienza", Piazzale Aldo Moro 2, I-00185 Roma, Italy*

(Received 26 April 2026; accepted 30 July 2026; published 26 August 2026)

We study the optical depth to reionization in a cosmological setting that includes backreaction from matter inhomogeneities, using the Buchert averaging formalism. We construct a spacetime model consisting of multiple inhomogeneous domains, hereafter referred to as the backreaction model, characterized by a set of parameters. We first examine how these parameters influence the computation of the optical depth to reionization, τ_{reion}. Next, we carry out a Markov chain Monte Carlo (MCMC) analysis based on the Pantheon+SH0ES type Ia supernova sample to infer the best-fit values of the model parameters, and then use these to evaluate τ_{reion}. We obtain $\tau_{\mathrm{reion}} = 0.0581^{+0.0105}_{-0.0096}$ (68% confidence limits). This result indicates that, when Pantheon+SH0ES data are used to constrain the model parameters, our backreaction model yields a value of τ_{reion} that aligns more closely with observational estimates than the value predicted by the standard cosmological model. We further demonstrate that the backreaction model leads to a modest reduction of the Hubble tension, while avoiding the need for exotic or nonstandard physics.

DOI: 10.1103/dgly-z27m

I. INTRODUCTION

Since its formulation, the ΛCDM (Λ cold dark matter) model has successfully explained numerous cosmological observations. However, in recent years, improved precision and consistency of observations of various cosmic phenomena [1–3] have revealed growing tensions between the theoretical predictions of the ΛCDM model and the observations [4–9]. The most statistically significant of these discrepancies is the Hubble tension—a disagreement of 4.7σ to 6.5σ [10–13] between two independent measurements of the Hubble constant, H_0. On the one hand, the Planck collaboration derives H_0 from high-redshift cosmic microwave background (CMB) observations combined with the assumptions of the ΛCDM model [1]. On the other hand, measurements from low-redshift late-time observations using type Ia supernovae calibrated with classical Cepheid variables [2,14,15] leads to persistent disagreement with the early Universe determination of H_0, thereby constituting the Hubble tension.

The ΛCDM model relies on the Friedmann-Lemaître-Robertson-Walker (FLRW) metric, which is fundamentally grounded in the cosmological principle, the assumption that the Universe exhibits statistical homogeneity and isotropy on large scales. However, recent large-scale structure (LSS) observations suggest the need to incorporate additional complexities beyond the standard cosmological framework. Although the Universe may indeed be uniform and isotropic at the largest scales, numerous astrophysical surveys have unveiled significant matter distribution inhomogeneities extending to substantial scales [16–21]. The deviations from homogeneity are statistically significant, with luminous red galaxy samples showing departures exceeding 3σ from ΛCDM mock catalogs on scales as large as $500h^{-1}$ Mpc [22]. The discovery of a giant arc of galaxies spanning approximately 1 Gpc (proper size at the present epoch) presents a notable challenge to the ΛCDM framework [23]. However, subsequent studies have questioned its cosmological significance [24–26].

The observed departures from the smooth, homogeneous Universe assumed in the ΛCDM paradigm suggest that incorporating the effects of inhomogeneities may be essential for accurate analyses of cosmological phenomena. The effect of local inhomogeneities on the dynamics at larger scales is generally termed as backreaction. Models of

[*]Contact author: shashankpandey7347@gmail.com
[†]Contact author: ruchika.science@usal.es
[‡]Contact author: shubhadeep.avg@gmail.com
[§]Contact author: archan@bose.res.in

backreaction that analyze the effect of matter distribution inhomogeneities on cosmological dynamics [27,28] systematically incorporate inhomogeneity effects into cosmological analyses through various averaging schemes [29–33]. Buchert introduced a particularly effective averaging procedure [34,35] focusing on scalar quantities defined on spacelike hypersurfaces. The Buchert averaging framework has subsequently been employed in numerous studies investigating how the backreaction of inhomogeneities affects cosmological dynamics, with particular attention to explaining the Universe's observed accelerated expansion [17,27,34–57]. Backreaction effects have also been applied to address other observational puzzles. For example, [58] argues that the backreaction from the inhomogeneous matter distribution could explain the Experiment to Detect Global Epoch of reionization Signal (EDGES) 21-cm signal observations without requiring exotic physics. Reference [59] investigates how 21-cm brightness temperature can be utilized to constrain the Hubble parameter within the context of an inhomogeneous cosmological model.

In this context, it may be noted that a recent work related to Dark Energy Spectroscopic Instrument (DESI) baryon acoustic oscillation (BAO) measurements [60] have reported a past phantomlike dark energy ($\omega(z) < -1$, where $\omega(z)$ is the equation of state of the dark energy) transitioning to nonphantomlike ($\omega(z) > -1$) today. This is accompanied by a decrease in the universe's acceleration, possibly leading to deceleration. This analysis is further supported by a recent study of supernova cosmology [61], which reports a significant tension ($> 9\sigma$) with the ΛCDM model. Such observations of a decelerating universe can be accounted for by backreaction models, without resorting to exotic or nonstandard physics [50,62]. Moreover, a two-parameter extension of the flat ΛCDM model that incorporates the effects of matter inhomogeneities on cosmological interpretations has been introduced recently [63], suggesting the possibility of addressing the Hubble tension through backreaction from the cosmic web structure, which could reconcile early and late-universe cosmological measurements.

Buchert's averaging procedure for evaluating backreaction effects from matter distribution inhomogeneities provides a promising theoretical framework for connecting spatially averaged quantities to observationally measurable phenomena, particularly redshift-distance relations [44,45,64–67]. Studies of electromagnetic wave propagation through inhomogeneous spacetime have revealed distinctive modifications to the redshift-distance relation arising from backreaction effects [44,45,66]. Analogous phenomena have been demonstrated for gravitational waves from compact binary systems propagating through inhomogeneous matter distributions [51,52]. Previous studies have examined the effects of inhomogeneous matter distribution on the Hubble tension with varying degrees of success [68–74]. Given these theoretical developments and their potential observational implications, we apply Buchert's averaging procedure to analyze another significant cosmological parametrization, viz., the optical depth to reionization in the Universe with an inhomogeneous matter distribution.

The reionization of the Universe is closely linked to the formation of the first stars and galaxies, which are the primary sources of ionizing photons. Reionization affects our ability to measure the CMB radiation as it propagates through the intergalactic medium. The optical depth to reionization, τ_{reion}, is a dimensionless quantity which provides a measure of the line-of-sight free-electron opacity to CMB radiation [75]. Cosmic reionization is a topic of significant importance in both astrophysics and cosmology and the parameter τ_{reion} plays a crucial role in its analysis. Determining τ_{reion} from observational data is therefore of strong interest [76–78], and may have a direct bearing on the tension between CMB and BAO measurements [79,80]. The Planck public-release PR3 results [1] provide the optical depth and reionization redshift as $\tau_{\mathrm{reion}} = 0.0544^{+0.0070}_{-0.0081}$, and $z_{\mathrm{reion}} = 7.68 \pm 0.79$. This value of τ_{reion} is for the base-ΛCDM model and is obtained from the TT, TE, EE + lowE spectra and is weakly dependent on the cosmological model. In [1], the value of z_{reion} is obtained by incorporating the tanh model of reionization with the τ_{reion} value (see Sec. II B). In the present study, we investigate τ_{reion} within a backreaction model.

In the present work, our approach considers a multidomain spacetime model that provides a more realistic representation of the actual Universe compared to the simplified two-domain toy models predominantly used in earlier backreaction studies [44,48–51]. The backreaction model considered here incorporates six parameters: four associated with matter distribution inhomogeneities, the dimensionless Hubble parameter h (where $H_0 = 100h\ \mathrm{km\,s^{-1}\,Mpc^{-1}}$), and n, representing the total number of subregions of each type. Following previous optimizations [58,62], we adopt $n = 100$. We explore the backreaction model as an alternative to the standard ΛCDM cosmological framework. We perform a Markov Chain Monte Carlo (MCMC) analysis to constrain the parameters of the backreaction model, using a low-redshift observational dataset which includes Pantheon+SH0ES (Supernova H0 for the equation of state) type Ia supernova data. We constrain the parameter h, thereby placing constraints on H_0 and enabling us to address the Hubble tension. Based on these constrained model parameters, we evaluate the τ_{reion} value and compare it with values obtained for the ΛCDM model for various observational datasets.

The paper is organized as follows. We briefly introduce the cosmological models that have been employed in this analysis in Sec. II A. We also briefly outline Buchert's averaging procedure and our multidomained backreaction model here. Next, we introduce a formalism to evaluate the optical depth to reionization in Sec. II B. We then present a multidomain analysis of the optical depth to reionization in the context of the multidomain backreaction model in

Sec. III. In Sec. IV, we use the Pantheon+SH0ES type Ia supernova dataset to constrain the backreaction model parameters and calculate the optical depth to reionization using the optimal parameter values. Finally, we summarize our results in Sec. V.

II. MODEL AND METHODOLOGY

A. Background cosmological models

1. ΛCDM *model*

The ΛCDM model is the current standard framework of cosmology. It assumes a homogeneous and isotropic Universe described by the FLRW metric, with dynamics governed by general relativity. The energy budget consists of radiation, baryonic matter, cold dark matter, and a cosmological constant Λ that drives late-time acceleration. The Hubble parameter in this model evolves with redshift as

$$H_{\Lambda\mathrm{CDM}}(z) = H_0\sqrt{\Omega_m(1+z)^3 + \Omega_r(1+z)^4 + \Omega_\Lambda}, \qquad (1)$$

where Ω_m, Ω_r, and Ω_Λ are the present-day density parameters for matter, radiation, and dark energy, respectively. Because of its simplicity and its success in reproducing a broad spectrum of observations, ΛCDM serves as the standard reference model against which alternative approaches, such as the backreaction framework, are evaluated.

2. *Backreaction model*

In this analysis, we utilize Buchert's averaging method tailored to a pressureless model (Buchert's backreaction formalism), explicitly referring to the dust universe model [34,81]. Buchert's backreaction framework streamlines the averaging process by focusing solely on scalar quantities. The division of spacetime is accomplished through flow-orthogonal hypersurfaces characterized by the line element [27,34]

$$ds^2 = -dt^2 + g_{ij}dX^i dX^j, \qquad (2)$$

where t is the proper time, X^i are Gaussian normal coordinates in the hypersurfaces and g_{ij} is the spatial three-metric of the hypersurfaces of constant t. The volume of a compact spatial domain $\mathcal{D}$ on these hypersurfaces is defined as

$$|\mathcal{D}|_g \coloneqq \int_{\mathcal{D}} d\mu_g, \qquad (3)$$

where $d\mu_g \coloneqq \sqrt{^{(3)}g(t,X^1,X^2,X^3)}dX^1dX^2dX^3$. Now, we define a dimensionless ("effective") scale factor

$$a_{\mathcal{D}}(t) \coloneqq \left(\frac{|\mathcal{D}|_g}{|\mathcal{D}_i|_g}\right)^{1/3}, \qquad (4)$$

normalized by the initial volume of the domain $|\mathcal{D}_i|_g$, which can be considered the domain's current volume, at the present time t_0. The average over a scalar quantity f is defined as

$$\langle f\rangle_{\mathcal{D}}(t) \coloneqq \frac{\int_{\mathcal{D}} f(t,X^1,X^2,X^3)d\mu_g}{\int_{\mathcal{D}} d\mu_g}. \qquad (5)$$

Using this averaging procedure and scalar parts of the Einstein equations, that is, the Hamiltonian constraint and the Raychaudhuri evolution equation for the expansion scalar, together with the continuity equation, gives us evolution equations [34]

$$3\frac{\ddot{a_{\mathcal{D}}}}{a_{\mathcal{D}}} = -4\pi G\langle\rho\rangle_{\mathcal{D}} + \mathcal{Q}_{\mathcal{D}} \qquad (6)$$

$$3H_{\mathcal{D}}^2 = 8\pi G\langle\rho\rangle_{\mathcal{D}} - \frac{1}{2}\langle\mathcal{R}\rangle_{\mathcal{D}} - \frac{1}{2}\mathcal{Q}_{\mathcal{D}} \qquad (7)$$

$$0 = \partial_t\langle\rho\rangle_{\mathcal{D}} + 3H_D\langle\rho\rangle_{\mathcal{D}}, \qquad (8)$$

where $\langle\rho\rangle_{\mathcal{D}}$, $\langle\mathcal{R}\rangle_{\mathcal{D}}$ and $H_{\mathcal{D}}$ are the averaged matter density, averaged spatial Ricci scalar and the Hubble parameter ($H_{\mathcal{D}} \coloneqq \dot{a_{\mathcal{D}}}/a_{\mathcal{D}}$) of the domain $\mathcal{D}$, respectively. $\mathcal{Q}_{\mathcal{D}}$ is called the kinematical backreaction and is defined as

$$\mathcal{Q}_{\mathcal{D}} \coloneqq \frac{2}{3}(\langle\theta^2\rangle_{\mathcal{D}} - \langle\theta\rangle_{\mathcal{D}}^2) - 2\langle\sigma^2\rangle_{\mathcal{D}}, \qquad (9)$$

where θ is the local expansion rate and $\sigma^2 \coloneqq 1/2\sigma_{ij}\sigma^{ij}$ is the squared rate of shear. The Hubble parameter $H_{\mathcal{D}}$ and $\langle\theta\rangle_{\mathcal{D}}$ are related by the relation $H_{\mathcal{D}} = 1/3\langle\theta\rangle_{\mathcal{D}}$. $\mathcal{Q}_{\mathcal{D}}$ is zero for an FLRW-like domain. The necessary condition of integrability connecting Eqs. (6) and (7) is given by

$$\frac{1}{a_{\mathcal{D}}^2}\partial_t(a_{\mathcal{D}}^2\langle\mathcal{R}\rangle_{\mathcal{D}}) + \frac{1}{a_{\mathcal{D}}^6}\partial_t(a_{\mathcal{D}}^6\mathcal{Q}_{\mathcal{D}}) = 0. \qquad (10)$$

In Eq. (10), a key aspect of the averaged equations is illustrated; it links the evolution of the averaged intrinsic curvature ($\langle\mathcal{R}\rangle_{\mathcal{D}}$) to the kinematic backreaction term ($\mathcal{Q}_{\mathcal{D}}$). This term represents the incorporation of matter inhomogeneities into the analysis. The interdependence of $\langle\mathcal{R}\rangle_{\mathcal{D}}$ and $\mathcal{Q}_{\mathcal{D}}$, alongside $\mathcal{Q}_{\mathcal{D}}$, signifies the deviation from homogeneity.

In the framework of the Buchert formalism, we adopt a particular method where groups of disjoint regions collectively define the global domain [17,27,40–56]. In this context, the global domain $\mathcal{D}$ is envisioned as being divided into subregions $\mathcal{F}_l$, each of which is composed of more fundamental spatial units $\mathcal{F}_l^{(\alpha)}$. Thus, in mathematical terms, we express this as $\mathcal{D} = \cup_l \mathcal{F}_l$, where $\mathcal{F}_l \coloneqq \cup_\alpha \mathcal{F}_l^{(\alpha)}$ and $\mathcal{F}_l^{(\alpha)} \cap \mathcal{F}_m^{(\beta)} = \varnothing$ for all $\alpha \neq \beta$ and $l \neq m$.

Average of a scalar-valued function f on the domain $\mathcal{D}$ is given by

$$\langle f\rangle := |\mathcal{D}|_g^{-1}\int_{\mathcal{D}} f d\mu_g = \sum_l |\mathcal{D}|_g^{-1}\sum_\alpha \int_{\mathcal{F}_l^{(\alpha)}} f d\mu_g = \sum_l \frac{|\mathcal{F}_l|_g}{|\mathcal{D}|_g}\langle f\rangle_{\mathcal{F}_l} = \sum_l \lambda_l \langle f\rangle_{\mathcal{F}_l}, \quad (11)$$

where

$$\lambda_l := \frac{|\mathcal{F}_l|_g}{|\mathcal{D}|_g} \quad (12)$$

is the volume fraction of the subregion $\mathcal{F}_l$ such that $\sum_l \lambda_l = 1$ and $\langle f\rangle_{\mathcal{F}_l}$ is the average of f on subregion $\mathcal{F}_l$. The scalar quantities ρ, $\mathcal{R}$, and $\mathcal{H}_{\mathcal{D}}$ are governed by Eq. (11), but $\mathcal{Q}_{\mathcal{D}}$, due to the presence of $\langle\theta\rangle_{\mathcal{D}}^2$-term, do not adhere to the above equation and instead follow

$$\mathcal{Q}_{\mathcal{D}} = \sum_l \lambda_l \mathcal{Q}_l + 3\sum_{l\neq m}\lambda_l\lambda_m (H_l - H_m)^2, \quad (13)$$

where $\mathcal{Q}_l$ and $\mathcal{H}_l$ are defined in subregion $\mathcal{F}_l$ in the same way as $\mathcal{Q}_{\mathcal{D}}$ and $\mathcal{H}_{\mathcal{D}}$ are defined in the domain $\mathcal{D}$. We can also define the scale factor a_l for a subregion $\mathcal{F}_l$. By definition, the different subregions are disjoint; therefore it follows that $|\mathcal{D}|_g = \sum_l |\mathcal{F}_l|_g$ and hence, using Eq. (4), we have

$$a_{\mathcal{D}}^3 = \sum_l \lambda_{l_i} a_l^3, \quad (14)$$

where $\lambda_{l_i} = \frac{|\mathcal{F}_{l_i}|_g}{|\mathcal{D}_i|_g}$ is the initial volume fraction which can also be taken as the volume fraction at present and can be represented as λ_{l_0}, where the subscript 0 stands for quantities calculated at the present time. Differentiating this relation twice with respect to the foliation time results in

$$\frac{\ddot{a}_D}{a_D} = \sum_l \lambda_l \frac{\ddot{a}_l(t)}{a_l(t)} + \sum_{l\neq m}\lambda_l\lambda_m (H_l - H_m)^2. \quad (15)$$

A model of multiple subregions. Here, using Buchert's backreaction framework, we consider a model of the Universe in which domain $\mathcal{D}$ comprises multiple underdense and overdense subregions. Similar models have been used in [62] to study the future evolution of the accelerating universe with multiple inhomogeneous domains and in [58] to analyze the 21-cm signal in the Universe with inhomogeneities. The underdense subregions have lower densities than the overdense subregions. The underdense subregions are modeled as almost-empty matter-dominated FLRW regions with very little matter (dust). The overdense subregions are modeled as matter-dominated FLRW models with matter (dust) content. The underdense subregions are taken to have Friedmann-like $1/a^2$ negative curvature, while the overdense subregions have Friedmann-like $1/a^2$ positive curvature. The time evolution of the scale factor of ith overdense subregions, a_{o_i} is given in terms of a development angle ϕ_{o_i} of the ith overdense subregion [82]

$$a_{o_i} = \frac{q_{o_{i,0}}}{2q_{o_{i,0}} - 1}(1 - \cos\phi_{o_i}) \quad (16)$$

$$t = t_0 \frac{(\phi_{o_i} - \sin\phi_{o_i})}{(\phi_{o_{i,0}} - \sin\phi_{o_{i,0}}),} \quad (17)$$

where $q_{o_{i,0}}$ and $\phi_{o_{i,0}}$ are respectively the deceleration parameter of the ith overdense subregion and the value of ϕ_{o_i} at time t_0, which is the present time. For an overdense region such as the one considered here, $q_{o_{i,0}}$ must be greater than $1/2$ [82]. Here, we have set $q_{o_{i,0}}$ to take values between $1/2$ and 1. The time t in Eq. (17) is the cosmic time, although for each overdense subregion, this t is a function of $(\phi_{o_{i,0}}, \phi_{o_i})$ ($\phi_{o_{i,0}}$ itself is a function of $q_{o_{i,0}}$). Therefore, each underdense subregion has a different evolution of t as a function of $(q_{o_{i,0}}, \phi_{o_i})$ but value of t_0 is the same across all overdense subregions as well as for the global domain, which is ensured by the specific form of Eq. (17). The time evolution of the scale factor of ith underdense subregions, a_{u_i} is given in terms of a development angle ϕ_{u_i} of the ith underdense subregion [82]

$$a_{u_i} = \frac{q_{u_{i,0}}}{1 - 2q_{u_{i,0}}}(\cosh\phi_{u_i} - 1) \quad (18)$$

$$t = t_0 \frac{(\sinh\phi_{u_i} - \phi_{u_i})}{(\sinh\phi_{u_{i,0}} - \phi_{u_{i,0}}),} \quad (19)$$

where $q_{u_{i,0}}$ and $\phi_{u_{i,0}}$ are, respectively, the deceleration parameter of the ith underdense subregion and the value of ϕ_{u_i} at time t_0, which is the present time. For an underdense region such as the one considered here, $q_{u_{i,0}}$ ranges from 0 to $1/2$ [82]. The time t in Eq. (19) is the cosmic time, although for each underdense subregion, this t is a function of $(\phi_{u_{i,0}}, \phi_{u_i})$ ($\phi_{u_{i,0}}$ itself is a function of $q_{u_{i,0}}$). Therefore, each underdense subregion has a different evolution of t as a function of $(q_{u_{i,0}}, \phi_{u_i})$, but the value of t_0 is the same across all underdense and overdense subregions as well as for the global domain which is ensured by the specific form of Eqs. (19) and (17). Since the values of t_0 and $H_{\mathcal{D}_0}$ are interrelated, one needs to fix either of them [57]. The value of t_0 is calculated using the procedure used in [58].

Note that a_{o_i} and a_{u_i} can be expressed in terms of the volume of the respective subregions using Eq. (4), which gives us

$$a_{o_i}(t) := \left(\frac{|\mathcal{D}|_{o_i}}{|\mathcal{D}_0|_{o_i}}\right)^{1/3}; \qquad a_{u_i}(t) := \left(\frac{|\mathcal{D}|_{u_i}}{|\mathcal{D}_0|_{u_i}}\right)^{1/3}, \quad (20)$$

where $|\mathcal{D}|_{o_i}$ is the volume of the ith overdense subregions at time t, $|\mathcal{D}_0|_{o_i}$ is the volume of the ith overdense subregion at time t_0 as was done in Eq. (4), and similarly for the case of the underdense subregions. Equations (4) and (20) require that at $t = t_0$, $a_{\mathcal{D}} = a_{o_i} = a_{u_i} = 1$, leading to

$$\cos\phi_{o_{i,0}} = \left(\frac{1}{q_{o_{i,0}}} - 1\right);$$
$$\cosh\phi_{u_{i,0}} = \left(\frac{1}{q_{u_{i,0}}} - 1\right). \tag{21}$$

For a given value of $q_{o_{i,0}}$ and $q_{o_{i,0}}$; $a_{o_i}(t)$ and $a_{u_i}(t)$ can be calculated using Eqs. (16)–(19) and (21). Then using Eq. (14), $a_{\mathcal{D}}(t)$ can be obtained provided λ_{l_0} which is the set of all $\lambda_{u_i,0}$ and $\lambda_{o_i,0}$, is known.

It may be noted that $a_{\mathcal{D}}$ can also be obtained from solving the second-order differential equation Eq. (15). Using Eqs. (16) and (18) in Eq. (15), we get

$$\frac{\ddot{a}_{\mathcal{D}}}{a_{\mathcal{D}}} = \left(\sum_i \lambda_{o_i}\frac{\ddot{a}_{o_i}}{a_{o_i}}\right) + \left(\sum_j \lambda_{u_j}\frac{\ddot{a}_{u_i}}{a_{u_i}}\right) + \left(\sum_k\sum_l \lambda_k\lambda_l(H_l - H_k)^2\right), \tag{22}$$

where, λ_{o_i} is the volume fraction of the ith overdense subregion, λ_{u_j} is the volume fraction of the jth underdense subregion, λ is the set of all λ_{o_i} and λ_{u_i} and H is respectively, the set of all H_{o_i} and H_{u_i}. The combined volume fraction of all the underdense subregions is given by λ_u, i.e., $\sum_i \lambda_{u_i} = \lambda_u$. Similarly, the total volume fraction of all the overdense subregions is given by $\sum_i \lambda_{o_i} = \lambda_o$. Clearly, $\lambda_o + \lambda_u = 1$. The evaluation of $a_{\mathcal{D}}$ obtained from these two methods is identical, as confirmed through our analysis.

The volume fraction of the ith overdense subregion can be written as

$$\lambda_{o_i} = \frac{|\mathcal{F}_{o_i}|_g}{|\mathcal{D}|_g} = \frac{a_{o_i}^3|\mathcal{F}_{o_i,0}|_g}{a_{\mathcal{D}}^3|\mathcal{D}_0|_g} = \lambda_{o_i,0}\frac{a_{o_i}^3}{a_{\mathcal{D}}^3}, \tag{23}$$

where t_0 is a reference time which can be taken as the present time, $|\mathcal{F}_{o_i}|_g$ is the volume of the ith overdense subregion, $|\mathcal{F}_{o_i,0}|_g$ is the volume of the ith overdense subregion at time t_0, $|\mathcal{D}_0|_g$ is the volume of the domain $\mathcal{D}$ at time t_0 and $\lambda_{o_i,0}$ is the volume fraction of the ith overdense subregion at time t_0. The present time (t_0) value of (λ_o, λ_u) is given by $(\lambda_{o,0}, \lambda_{u,0})$ which we have taken to be (0.09, 0.91) [27].

In this backreaction model, we consider the present time volume fraction of ith underdense subregion, $\lambda_{u_i,0}$ to have a Gaussian distribution within the allowed range of $q_{u_{i,0}}$ from 0 to 1/2, given by

$$\lambda_{u_i,0} = \frac{N_u}{\sigma_u\sqrt{2\pi}}e^{-(q_{u_{i,0}}-\mu_u)^2/2\sigma_u^2}, \tag{24}$$

where N_u is a normalization constant which ensures that $\sum_i \lambda_{u_i,0} = \lambda_{u,0} = 0.91$, μ_u is the mean value of $q_{u_{i,0}}$ and σ_u is the standard deviation of $q_{u_{i,0}}$. Therefore, each ith underdense subregion is associated with a particular value of $q_{u_{i,0}}$ and $\lambda_{u_i,0}$ such that $q_{u_{i,0}}$ varies from 0 to 1/2 across the i number of underdense subregions and $\sum_i \lambda_{u_i,0} = 0.91$. Hence, this model's allowed range for μ_u is also from 0 to 1/2. And we are imposing the allowed range for σ_u from 0.01 to 0.09.

The present-time volume fraction of ith overdense subregion, $\lambda_{o_i,0}$ is considered to have a Gaussian profile within the allowed range of $q_{o_{i,0}}$ from 1/2 to 1 given by

$$\lambda_{o_i,0} = \frac{N_o}{\sigma_o\sqrt{2\pi}}e^{-(q_{o_{i,0}}-\mu_o)^2/2\sigma_o^2}, \tag{25}$$

where N_o is a normalization constant which ensures that $\sum_i \lambda_{o_i,0} = \lambda_{u,0} = 0.09$, μ_o is the mean value of $q_{o_{i,0}}$ and σ_o is the standard deviation of $q_{o_{i,0}}$. In this case, each ith overdense subregion is associated with a particular value of $q_{o_{i,0}}$ and $\lambda_{o_i,0}$, where $q_{o_{i,0}}$ lies within the range 1/2 to 1 across the i number of overdense subregions and $\sum_i \lambda_{o_i,0} = 0.09$. Hence, this model's allowed range for μ_o is also from 1/2 to 1. And we are imposing the allowed range for σ_o from 0.01 to 0.09. The volume fraction of the ith underdense subregion at a time t, λ_{u_i} is related to the volume fraction at present time t_0 by

$$\lambda_{u_i} = \lambda_{u_i,0}\left(\frac{1 - \sum_i \lambda_{o_i}}{1 - \sum_i \lambda_{o_i,0}}\right). \tag{26}$$

We employed the Gaussian distribution to characterize the current volume fraction for different subregions. To gain a genuine understanding of the physical distribution, extensive galactic surveys are required to map how matter is spread throughout the Universe. While surveys have examined the local Universe, no studies have been conducted for the redshifts pertinent to our analysis. In the absence of these surveys, we assume a normal distribution, as it is a standard choice known to model unbiased physical conditions effectively. The Gaussian distribution is a familiar and widely utilized tool in various physical studies.

Using Eq. (13), the kinematical backreaction term for the domain $\mathcal{D}$ for the backreaction model effectively becomes

$$\mathcal{Q}_{\mathcal{D}} = \sum_i \lambda_{o_i}\mathcal{Q}_{o_i} + \sum_j \lambda_{u_j}\mathcal{Q}_{u_j} + 3\sum_{l\neq m}\lambda_l\lambda_m(H_l - H_m)^2, \tag{27}$$

where $\mathcal{Q}_{o_i}$ is the kinematical backreaction term for the ith overdense subregion, $\mathcal{Q}_{u_i}$ is for the ith underdense subregion. The summation in the last term runs over the sets of all λ_{o_i}, λ_{u_i}, H_{o_i}, and H_{u_i}. The subregions are also governed by this coupling of the kinematical backreaction term to the Ricci scalar [Eq. (10)]. Therefore, by selectively choosing the curvatures of the subregions (FLRW-like), we can make the respective kinematical backreaction terms for these subregions equal to zero [27,28]. Hence, in this case, the global kinematical backreaction is governed by only the interplay of the subdomain Hubble evolutions and volume fractions [third term of Eq. (27)]. Note that the above assumptions are made in the context of the present model. On the other hand, if the subdomains are endowed with dynamical curvature, other intricate effects could arise through kinematical backreaction, as may also happen in a more general case where the subregions may not necessarily be FLRW. Obtaining the values of $\lambda_{o_i,0}$ and $\lambda_{u_i,0}$ from Eqs. (25) and (24) respectively, and using these in Eqs. (23) and (26) gives us λ_{o_i} and λ_{u_i}. Hubble parameters for the subregions can be obtained from Eqs. (16)–(19). We can then use Eq. (22) to get $a_{\mathcal{D}}(t)$ and $H_{\mathcal{D}}(t)$.

We next relate these quantities calculated theoretically from the backreaction model with observational quantities (redshift and angular diameter distance by using the covariant scheme [64,65], given by

$$1+z=\frac{1}{a_{\mathcal{D}}} \tag{28}$$

$$H_{\mathcal{D}}\frac{d}{dz}\left((1+z)^2 H_{\mathcal{D}}\frac{dD_A}{dz}\right)=-4\pi G\langle\rho\rangle_{\mathcal{D}}D_A. \tag{29}$$

Equation (28) relates $a_{\mathcal{D}}(t)$ with the cosmological redshift $z(t)$ and Eq. (29) relates the angular diameter distance D_A with $\langle\rho\rangle_{\mathcal{D}}$ and $H_{\mathcal{D}}$. Here, we use Eq. (28) to obtain $z(t)$ from $a_{\mathcal{D}}(t)$. We can thus evaluate $H_{\mathcal{D}}(z)$ using $H_{\mathcal{D}}(t)$ from Eq. (22) and $z(t)$ from Eq. (28). This particular model has been characterized thoroughly in [58].

In Fig. 1, the average density parameters are plotted as a function of the redshift in the redshift range ($z<30$). (See Appendix for the calculation of these average density parameters). The density parameter associated with kinematical backreaction, $\mathcal{Q}_{\mathcal{D}}$, plays a significant role in our backreaction model at late redshifts (around $z=5$, as seen in the inset), embodying the departure from FLRW behavior in our framework. The $\mathcal{Q}_{\mathcal{D}}$ term becomes negligible at large redshifts, which can be seen from the corresponding plot in Fig. 1. The term $\Omega_{\mathcal{Q}}^{\mathcal{D}}$ going to zero at high redshifts (or at early times) shows that our model can mimic an FLRW model at early times. At early times, the under- and overdense regions have opposite curvature sign, but as can be seen from Fig. 1, the density parameter for curvature is very small at early times in comparison to the density parameter of matter. Therefore, the presence of curvature does not play a significant role at early times. Curvature becomes significant only at late times.

While the backreaction model agrees with FLRW predictions at high redshift, it diverges from FLRW behavior at late times (low redshift). Since we fix the present-day cosmological parameters as boundary conditions for both the ΛCDM and backreaction frameworks and then evolve the system backward in time, the reconstructed past evolution of the Hubble parameter differs between the two scenarios. This mismatch in the backward evolution is what accounts for the difference between our ΛCDM-based results and those from the backreaction analysis.

B. Formulation of optical depth

The optical depth τ is defined as the integral of the electron density times the Thomson cross section over the geometrical path length between the present redshift and the redshift of reionization. It can be expressed as [75]

$$\tau(t)=\sigma_T\int_t^{t_0} n_e(t)c\,dt, \tag{30}$$

where n_e is the electron number density, $\sigma_T=6.65\times10^{-29}\ m^2$ is the Thomson scattering cross section, and t_0 is the present time.

To express this in terms of the redshift, we define the ionization fraction as $\chi(z)=n_e(z)/n_H(z)$ [1], where $n_H(z)$ is the number density of hydrogen nuclei. The number density of hydrogen nuclei evolves as

$$n_H(z)=n_{H,0}(1+z)^3, \tag{31}$$

where $n_{H,0}$ is the present-day value of $n_H(z)$. The time-redshift relation is

$$\frac{dz}{dt}=-(1+z)H(z). \tag{32}$$

Substituting into Eq. (30), the optical depth becomes

$$\tau(z)=n_{H,0}c\sigma_T\int_0^z(1+z')^2\frac{\chi(z')}{H(z')}dz'. \tag{33}$$

Assuming a primordial helium fraction of 24% [83], we have $n_H(z)=0.76n_B(z)$, where $n_B(z)$ is the baryon number density. Now, $n_{H,0}=0.76n_{B,0}$, where $n_{B,0}$ is the present-day value of $n_B(z)$ and is related to the baryon density parameter Ω_B via

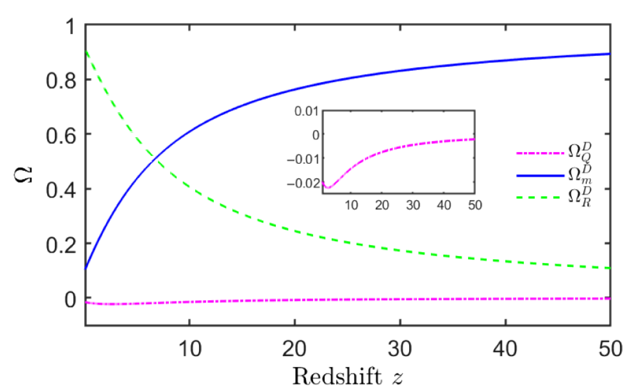

FIG. 1. Plot of averaged density parameters, $\Omega_m^{\mathcal{D}}$ and $\Omega_{\mathcal{Q}}^{\mathcal{D}}$ as a function of redshift, z. The values of the parameters are chosen as: $\mu_u=0.01$, $\sigma_u=0.01$, $\mu_o=0.99$ and $\sigma_o=0.01$. The inset shows the magnified plot for $\Omega_{\mathcal{Q}}^{\mathcal{D}}$, the density parameter for kinematical backreaction term $\mathcal{Q}_{\mathcal{D}}$.

$$\Omega_B = \frac{8\pi G}{3H_0^2} m_p n_{B,0}, \tag{34}$$

where m_p is the proton mass and $H_0 = 100h\ \mathrm{km\,s^{-1}\,Mpc^{-1}}$ is the Hubble constant. Here, we have used the PR3 release (Planck VI 2018) constrained value of $\Omega_b h^2 = 0.0224$ [1] to calculate $n_{B,0}$. For simplicity, both helium and hydrogen are assumed to be fully ionized.

We denote the total integrated optical depth to reionization as $\tau_{\rm reion}$, and it is given by [1]

$$\tau_{\rm reion} = n_{H,0} c \sigma_T \int_0^{z_{\max}} (1+z')^2 \frac{\chi(z')}{H(z')} dz', \tag{35}$$

where $z_{\max} = 50$, which is early enough to capture the full expected contribution from reionization.

The computation of the $\tau_{\rm reion}$ [the integral in Eq. (35)] relies on two fundamental ingredients: (i) the evolution of the Hubble parameter $H(z)$, determined by the underlying cosmological model, and (ii) the ionization fraction $\chi(z)$, specified by the reionization model. In this work, these two components are consistently combined within a unified pipeline: the cosmological sector provides the background expansion history as an input to the integral, while the reionization module computes the corresponding ionization fraction. The two parts are interfaced at the background evolution level, ensuring a coherent evaluation of the optical depth.

We consider two cosmological scenarios:

(i) the standard ΛCDM model, and

(ii) the multidomained backreaction model.

In both cases, the background expansion history is combined with the tanh reionization parametrization [1,84] to model the ionization fraction and compute the corresponding optical depth.

Each of these cosmological models is combined with the tanh reionization model [1,84]

$$\chi(z) = \frac{1 + n_{He}/n_H}{2}\left[1 + \tanh\left(\frac{y(z_{\rm reion}) - y(z)}{\Delta y}\right)\right], \tag{36}$$

where $y(z) = (1+z)^{3/2}$, $\Delta y = \frac{3}{2}(1+z_{\rm reion})^{1/2}\Delta z$, and $\Delta z = 0.5$. Throughout this study, we have used $z_{\rm reion} = 7.68$, unless otherwise stated (see Sec. II C).

We then analyze two distinct scenarios:

$$(\Lambda\mathrm{CDM} + \tanh), \qquad (\mathrm{backreaction} + \tanh).$$

For the evaluation of the (backreaction + tanh) scenario, the scalar quantities appearing in Eqs. (32)–(35) are substituted by their corresponding averaged counterparts. Using $H_{\mathcal{D}}(z)$ derived from the backreaction formalism and $\chi(z)$ from the reionization prescription, we compute $\tau_{\rm reion}$ via Eq. (35). This calculation is performed for both cosmological models (ΛCDM and backreaction), each paired with the tanh reionization prescription. Hence, two distinct values of $\tau_{\rm reion}$ are obtained and compared with the observational results.

C. Observational values of optical depth to reionization

In the Planck XIII 2015 (PR2) release [85], 68% confidence limits for the base ΛCDM model from Planck CMB power spectra, in combination with lensing reconstruction "lensing" and external data "ext," BAO + JLA + H_0, are given as (here, tanh prescription of ionization fraction is not used)

$$\tau_{\rm reion} = 0.066 \pm 0.012, \quad \text{and} \quad z_{\rm reion} = 8.8^{+1.2}_{-1.1}$$
$$(68\%\mathrm{TT,TE,EE} + \mathrm{lowP} + \mathrm{lensing} + \mathrm{ext}). \tag{37}$$

The Planck 2018 legacy release [Planck V 2018 (PR3)] [86] cites $\tau = 0.063 \pm 0.020$ as inferred from Low Frequency Instrument (LFI) data and 0.0506 ± 0.0086 from High Frequency Instrument (HFI) data.

In the Planck collaboration PR3 release [Planck VI 2018 (PR3)] [1], the optical depth is well constrained by the large-scale polarization measurements from the Planck HFI, with the joint constraint

$$\tau_{\rm reion} = 0.0544^{+0.0070}_{-0.0081} \quad (68\%\mathrm{TT,TE,EE} + \mathrm{lowE}), \tag{38}$$

and with the tanh reionization prescription, this implies a midpoint redshift of reionization

$$z_{\rm reion} = 7.68 \pm 0.79 \quad (68\%\mathrm{TT,TE,EE} + \mathrm{lowE}). \tag{39}$$

In the same release, the base-ΛCDM model from Planck CMB power spectra, in combination with CMB lensing reconstruction and BAO [1], gives

$$\tau_{\rm reion} = 0.0561 \pm 0.0071, \quad \text{and} \quad z_{\rm reion} = 7.82 \pm 0.71$$
$$(68\%\mathrm{TT,TE,EE} + \mathrm{lowE} + \mathrm{lensing} + \mathrm{BAO}). \tag{40}$$

Assuming the ΛCDM cosmological model and combining the Planck large-scale temperature likelihood with the high-l temperature and polarization likelihood, [77] derives a value of $\tau_{\rm reion} = 0.059 \pm 0.006$ (68% confidence level), which implies a reionization midpoint (assuming tanh parametrization) at $z_{\rm reion} = 8.14 \pm 0.61$ (68% confidence level).

Through further reprocessing of the Planck large-scale polarization measurements, [87] obtains a revised value for the reionization optical depth of $\tau_{\rm reion} = 0.051 \pm 0.006$.

Relative to the previous Planck cosmological analysis in [1], the constraints reported in [88] are more stringent, without any significant shifts in the central values. The reionization optical depth is now measured to a precision of a few percent, yielding $\tau_{\rm reion} = 0.058 \pm 0.006$.

In [89], estimates based on the Cosmology Large Angular Scale Surveyor (CLASS) 90 GHz data correlated with Planck data (Planck PR4, [87]) give $\tau_{\rm reion} = 0.058^{+0.018}_{-0.019}$. In [90], Atacama Cosmology Telescope (ACT) DR6 data in combination with Planck, lensing, and BAO data give $\tau_{\rm reion} = 0.0632^{+0.0055}_{-0.0066}$.

These observational constraints are shown in Fig. 8 for comparison. For the purposes of our analysis, we adopt as fiducial reference values those reported in Eqs. (38) and (39), which serve as the baseline constraints throughout this work.

III. EXPLORATION OF PARAMETER SPACE

Before performing a complete statistical comparison with observational data, we first explore the sensitivity of the optical depth of reionization $\tau_{\rm reion}$ to variations in the parameters of the backreaction model. This preliminary analysis allows us to identify the approximate ranges of parameters that yield values of $\tau_{\rm reion}$ compatible with Planck VI 2018 (PR3) constraints ($\tau_{\rm reion} = 0.0544^{+0.0070}_{-0.0081}$) [1].

The backreaction model employed here is characterized by six parameters: $(\mu_u, \sigma_u, \mu_o, \sigma_o, h, n)$. Following earlier work [58,62], we fix $n = 100$ and adopt $h = 0.7$ unless otherwise stated, leaving four free parameters $(\mu_u, \sigma_u, \mu_o, \sigma_o)$ that describe the matter distribution across underdense and overdense subregions. Figures 2–5 present the dependence of $\tau_{\rm reion}$ on these parameters, as well as on h in both ΛCDM and the backreaction model.

These plots are not intended as best-fit constraints, but rather as an illustration of how different physical ingredients of the model affect the reionization optical depth. The following section will confront the model predictions with observational data through a χ^2 analysis. We have used $z_{\rm reion} = 7.68$ in the analysis for this section.

Figure 2 displays $\tau_{\rm reion}$ for different values of the inhomogeneity parameters μ_o, μ_u, σ_o, and σ_u, while maintaining $n = 100$ and $h = 0.7$ as fixed values. All these plots contain the tanh model of reionization (blue line). Each subplot examines the impact of a single parameter on the reionization optical depth, varying it independently while holding the remaining three parameters constant. Specifically, panel (a) varies μ_o with $\sigma_o = \sigma_u = 0.01$ and $\mu_u = 0.09$ held fixed, panel (b) examines σ_o variation with $\mu_o = 0.99$, $\sigma_u = 0.01$, and $\mu_u = 0.08$ kept constant, panel (c) shows μ_u variation with $\sigma_o = \sigma_u = 0.01$ and $\mu_o = 0.95$ fixed, and panel (d) investigates σ_u variation with $\sigma_o = 0.01$, $\mu_o = 0.99$, and $\mu_u = 0.07$ held constant. These parameters (μ_o, μ_u, σ_o, σ_u) characterize the inhomogeneous matter distribution in the backreaction model, allowing us to assess how matter clustering affects the reionization process. The Hubble parameter is set to $H_0 = 100h$ km s^{-1} Mpc^{-1} with $h = 0.7$. The dashed black line indicates the Planck VI 2018 (PR3) measured value of $\tau_{\rm reion} = 0.054$, while the gray band represents the corresponding 68% confidence interval. The analysis reveals that variations in μ_u produce the most pronounced changes in $\tau_{\rm reion}$ among the four inhomogeneity parameters examined. This arises from the fact that, at the present time in our model, underdense subregions occupy 91% of the total volume and therefore associated parameters play a significant role in determining the values of various cosmological quantities.

In Fig. 3, $\tau_{\rm reion}$ for varying values of h has been plotted for the ΛCDM and the backreaction model. In subplot (a), the cosmological model is the ΛCDM model, while in subplot (b) it is the backreaction model. Both plots have been generated for the tanh model of reionization (blue line). For subplot (b), the value of the four backreaction model parameters $(\mu_u, \sigma_u, \mu_o, \sigma_o)$ has been fixed at (0.01, 0.01, 0.65, 0.01). These values were chosen by taking Fig. 2 into consideration. It can be seen from the figure that, for the employed combination of backreaction model parameters, the Planck reported value of $\tau_{\rm reion}$ can be obtained by the backreaction model (subplot b) for comparatively larger values of h than in the ΛCDM model (subplot a). In comparison to the ΛCDM model, $\tau_{\rm reion}$ for the backreaction model falls within the 68% confidence interval of the value reported by Planck for a narrower range of h.

Figure 4 presents correlation plots illustrating the variation of $\tau_{\rm reion}$ in the μ_o-σ_o parameter space for the tanh reionization model [subplots (a)–(d)]. We have used $z_{\rm reion} = 7.68$ and $h = 0.7$ in this analysis. The parameter μ_o spans the range 0.5–1.0 along the horizontal axis, while σ_o varies between 0.01–0.09 along the vertical axis. The color scheme represents the magnitude of $\tau_{\rm reion}$ according to the scale shown in the color bar. It varies from 0.025 to 0.065 for the range of backreaction model parameters employed here. Four different combinations of (μ_u, σ_u) values are examined across the subplots to assess their influence on the optical depth calculation.

Subplots (a) and (b) correspond to $(\mu_u, \sigma_u) = (0.01, 0.01)$ and (0.01, 0.09), respectively. The results demonstrate that subplot (a) yields systematically higher $\tau_{\rm reion}$ values compared to subplot (b), while both subplots exhibit minimal internal variation across the μ_o-σ_o parameter space. This behavior indicates that variations in the overdense region parameters (μ_o, σ_o) exert negligible influence on $\tau_{\rm reion}$ when (μ_u, σ_u) are held constant. Conversely, the substantial difference between subplots (a) and (b) highlights the significant impact of σ_u on the optical depth calculation for smaller values of μ_u. Subplots (c) and (d), corresponding to $(\mu_u, \sigma_u) = (0.49, 0.01)$ and (0.49, 0.09) respectively, exhibit markedly lower $\tau_{\rm reion}$ values compared to subplots (a) and (b). The transition from $\sigma_u = 0.01$ to $\sigma_u = 0.09$ while maintaining $\mu_u = 0.49$ produces minimal variation in $\tau_{\rm reion}$. This observation shows that at large values of μ_u, the effect of variation of σ_u on the value of $\tau_{\rm reion}$ is negligible. Notably, the Planck VI 2018 (PR3) reported value of $\tau_{\rm reion}$ is achieved within the parameter range explored in subplot (a). From Fig. 2, it can be seen that to achieve Planck's reported value of $\tau_{\rm reion}$, μ_u and σ_u both need to be on the lower end of their allowed range. In subplot (a), both μ_u and σ_u are at the lower end of their allowed range; hence, Planck's reported value is achieved in this subplot.

The comparison between subplots (a) and (c), where σ_u remains constant while μ_u varies, reveals that changes in μ_u

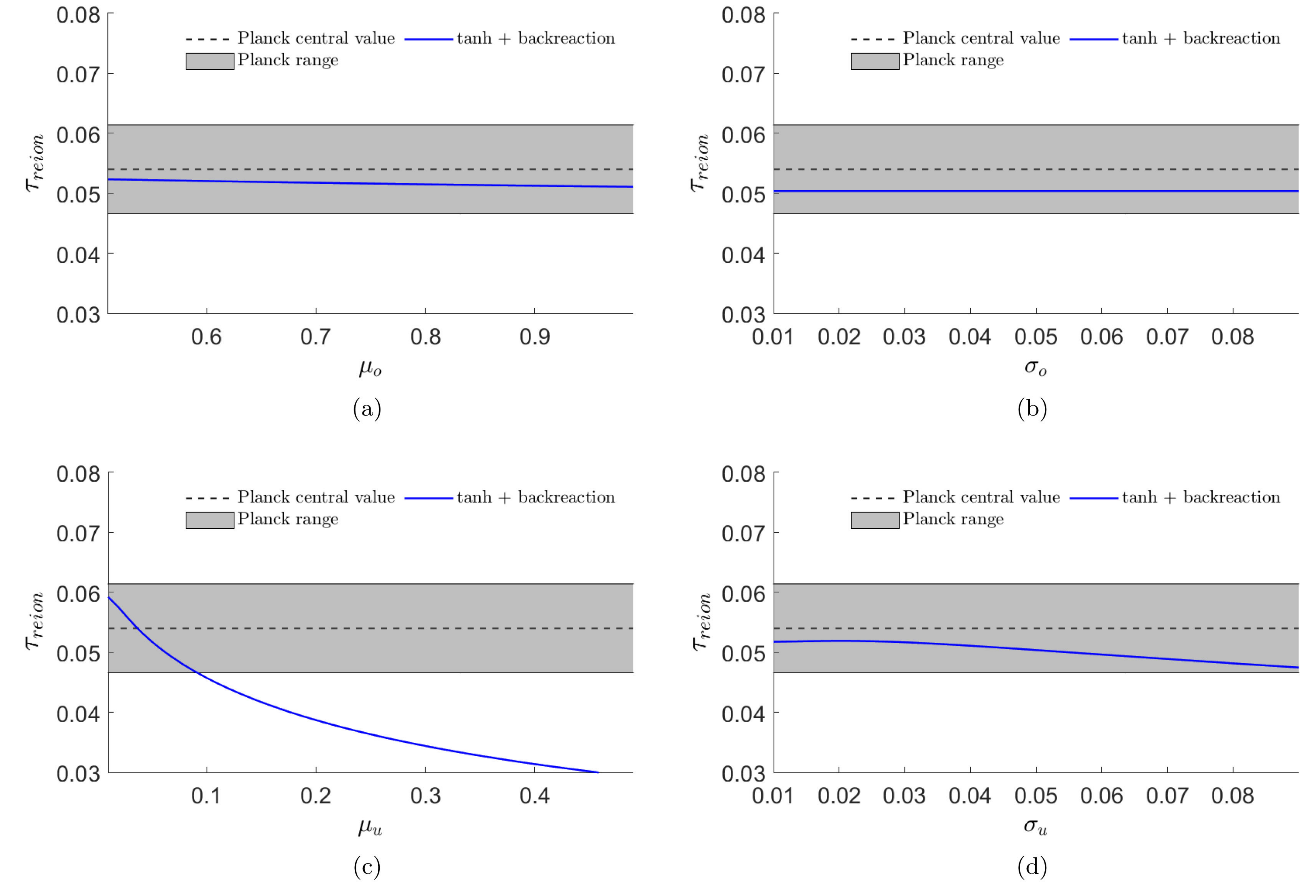

FIG. 2. Plots of $\tau_{\rm reion}$ for the backreaction model as a function of z. The backreaction model has six parameters. We have fixed two, $n = 100$ and $h = 0.7$. The other four parameters that can be varied are: μ_u, σ_u, μ_o, σ_o. In (a) μ_o is varied with $\sigma_o = \sigma_u = 0.01$ and $\mu_u = 0.09$ fixed. In (b) σ_o is varied with $\mu_o = 0.99$, $\sigma_u = 0.01$ and $\mu_u = 0.08$ fixed. In (c), μ_u is varied with $\sigma_o = \sigma_u = 0.01$ and $\mu_o = 0.95$ fixed. In (d), σ_u is varied with $\sigma_o = 0.01$, $\mu_o = 0.99$ and $\mu_u = 0.07$ fixed. The value of H_0 (Hubble parameter at present) used is $100h$ km s^{-1} Mpc^{-1} where $h = 0.7$. The dashed black line and the gray band show the Planck reported value of 0.054 and the 68% confidence interval. We have used $z_{\rm reion} = 7.68$.

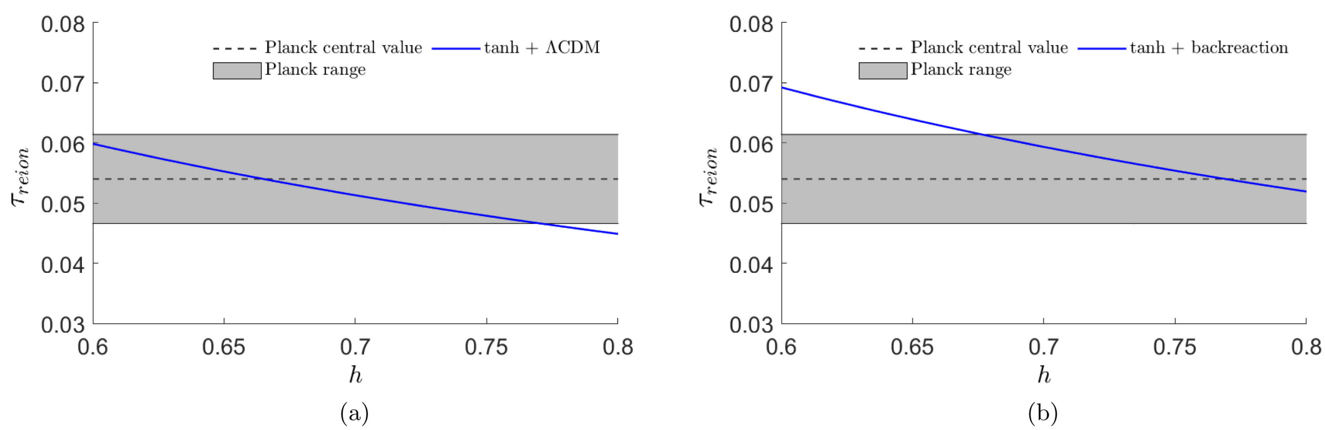

FIG. 3. Subplot (a) is the plot of τ for varying values of h for ΛCDM model. Subplot (b) is for the backreaction model. The gray dashed line shows the Planck reported value of 0.054. In subplot (b), the value of the four backreaction parameters $(\mu_u, \sigma_u, \mu_o, \sigma_o)$ has been fixed at (0.01, 0.01, 0.65, 0.01). The dashed black line and the gray band show the Planck reported value of 0.054 and the 68% confidence interval. We have used $z_{\rm reion} = 7.68$ in this analysis.

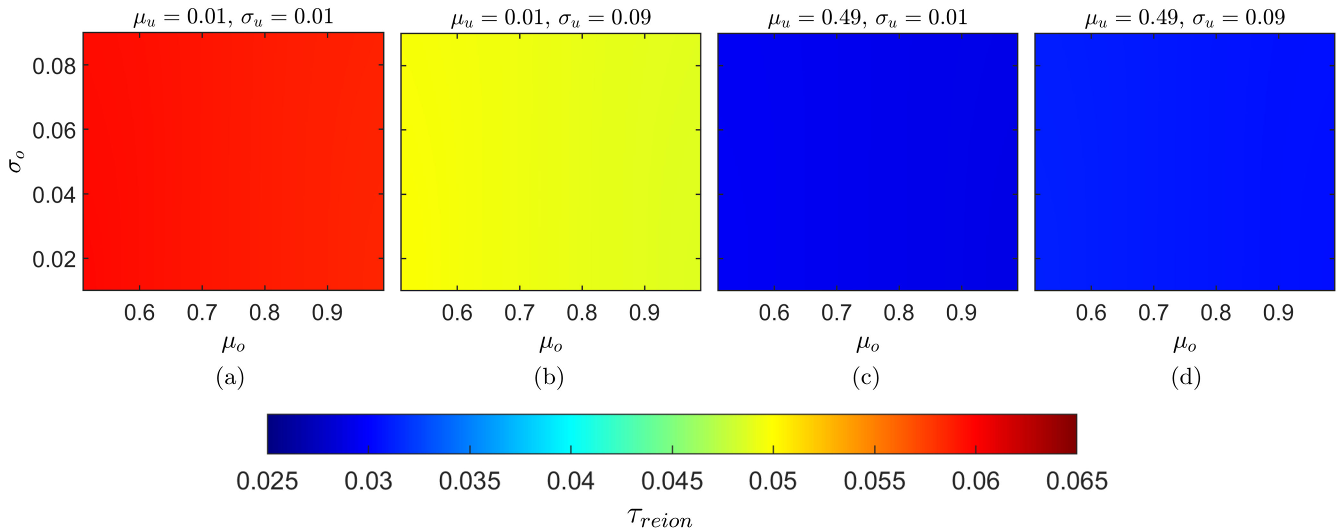

FIG. 4. Color coded representation of τ_{reion} in the μ_o-σ_o plane for the tanh model of reionization. For subplots: (a) $\mu_u = 0.01$, $\sigma_u = 0.01$; (b) $\mu_u = 0.01$, $\sigma_u = 0.09$; (c) $\mu_u = 0.49$, $\sigma_u = 0.01$; (d) $\mu_u = 0.49$, $\sigma_u = 0.09$.

produce more substantial variations in τ_{reion} than equivalent changes in σ_u [e.g., subplots (a) and (b)]. These findings collectively demonstrate that underdense region parameters, particularly μ_u, dominate in governing the global reionization optical depth. In contrast, the overdense region parameters exhibit limited influence on the overall dynamics.

In Fig. 5, the variation of τ_{reion} for the tanh model of reionization [subplots (a)–(d)] in the μ_u-σ_u plane is shown for different sets of values of (μ_o, σ_o) using a contour plot. We have used $z_{\text{reion}} = 7.68$ and $h = 0.7$ in this analysis. The value of μ_u varies in the range of 0–0.5 along the x-axis while σ_u is varied along the y-axis in the range of 0.01–0.09. The color scheme represents the magnitude of τ_{reion} according to the scale shown in the color bar. It varies from 0.025 to 0.06 for the range of backreaction model parameters employed here. In subplots (a) and (b) of the figures, μ_o is fixed at 0.51, and σ_o has the values of 0.01 and 0.09, respectively. In subplots (c) and (d) of the figures, μ_o is fixed at 0.99 while σ_u has the values of 0.01 and 0.09, respectively. These figures also highlight the insignificance of overdense parameters: all four subplots are similar, so changing them does not significantly affect the output. The only change in the plots is due to variation in the parameters (μ_u, σ_u) associated with the underdense subregions. These observations agree with the inferences from Fig. 2.

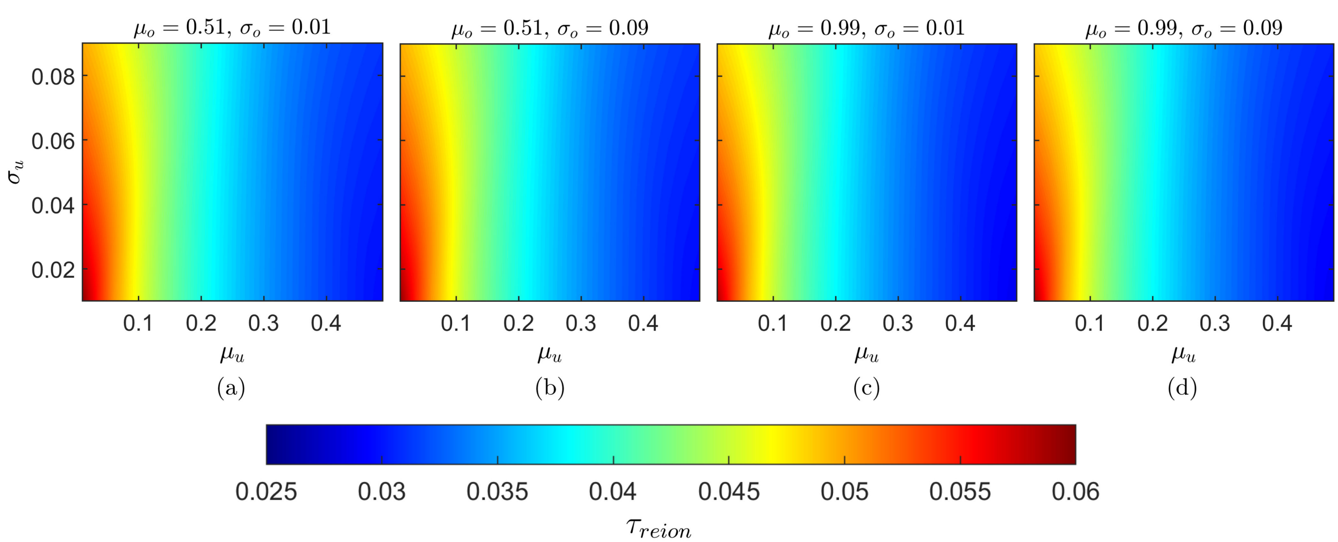

FIG. 5. Color coded representation of τ_{reion} in the μ_u-σ_u plane for the tanh model of reionization. For subplots: (a) $\mu_o = 0.51$, $\sigma_o = 0.01$; (b) $\mu_o = 0.51$, $\sigma_o = 0.09$; (c) $\mu_o = 0.99$, $\sigma_o = 0.01$; (d) $\mu_o = 0.99$, $\sigma_o = 0.09$.

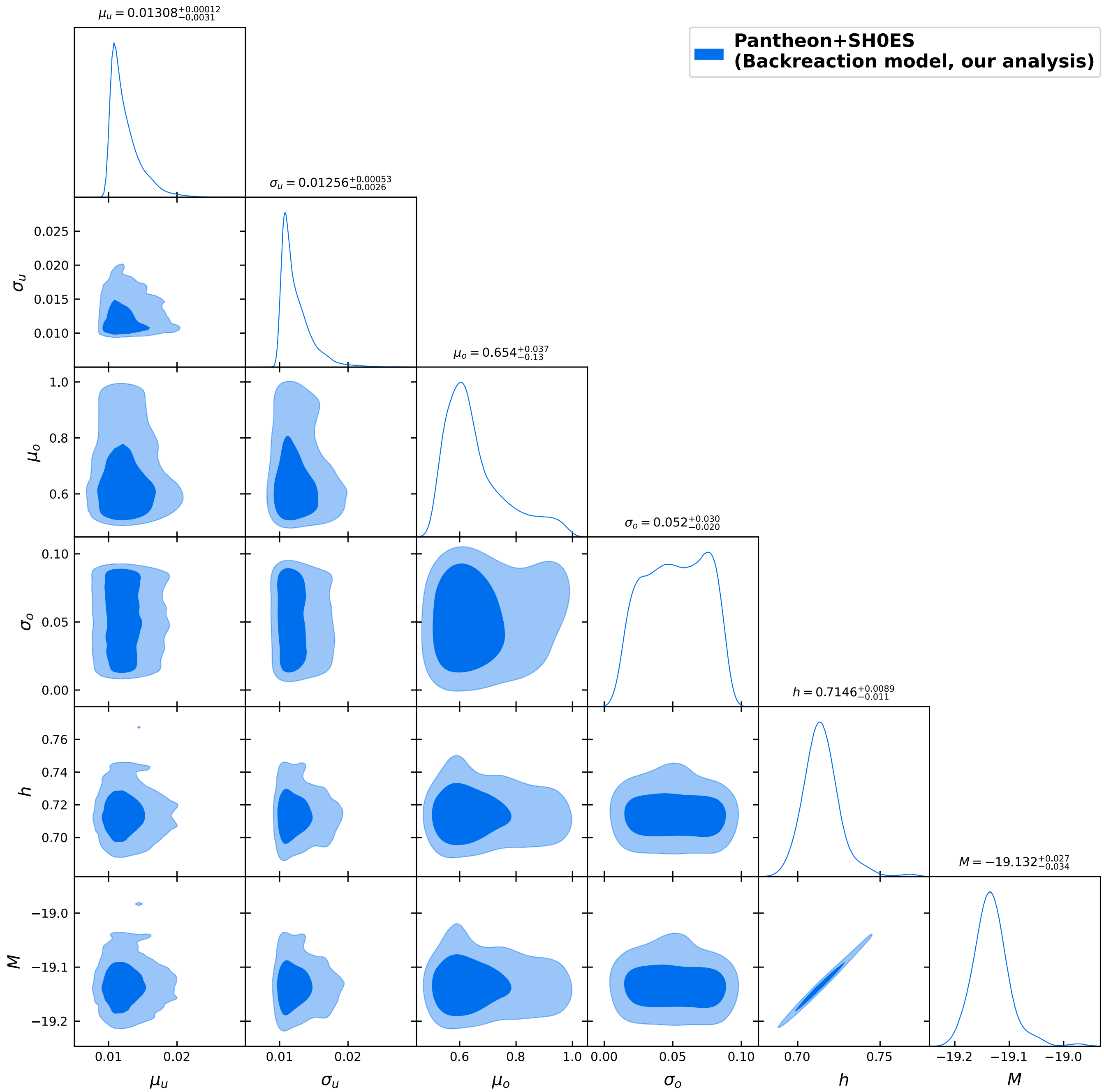

FIG. 6. Corner plot showing the MCMC result for the backreaction model carried out using the observational results of the Pantheon +SH0ES supernova Ia data [2,14]. The diagonal plots show the marginalized posterior densities for each parameter. Here, we have also included M, the fiducial magnitude of SN Ia, as one of the parameters.

IV. OBSERVATIONAL DATA AND CHI-SQ ANALYSIS

We now examine the backreaction model against observational data to determine the optimal parameter values. A Bayesian analysis is conducted to compare our theoretical predictions with the Pantheon+SH0ES type Ia supernova distance modulus versus redshift data [2,14]. To facilitate this comparison between the backreaction model and observational data, we require a framework that relates the theoretical quantities to the observational ones. We employ the covariant scheme described specifically in Eqs. (28) and (29). The first equation of the covariant scheme Eq. (28) establishes the relationship between the theoretically calculated scale factor $a_{\mathcal{D}}$ from the backreaction model and the cosmological redshift. The second equation Eq. (29) connects the theoretically calculated average density $\langle\rho\rangle_{\mathcal{D}}$ from the backreaction model to the observational quantity, specifically the angular diameter distance D_A. Using standard cosmological distance relations, we can subsequently calculate the distance modulus from this angular diameter distance.

To proceed with the supernova analysis, we utilize the standard distance modulus formulation for SN Ia [2,14,91]

$$\mu = m_B + \alpha x_1 - \beta c - M - \delta_{\mu-\mathrm{bias}}, \tag{41}$$

where $m_B \equiv -2.5\log_{10}(x_0)$, where x_0 is the overall amplitude of the light curve, x_1 is the stretch parameter corresponding to the width of the light curve, c is the color of the light curve and α and β are global nuisance parameters that associate stretch and color, respectively, with luminosity. We have used $\alpha = 0.148$ and $\beta = 3.112$ [2] in this analysis. M is the fiducial absolute magnitude of an SN Ia. $\delta_{\mu-\mathrm{bias}}$ is the bias correction derived from simulations needed to account for selection effects and other issues in discovery. In this analysis, we have also included M [Eq. (41)], the fiducial magnitude of SN Ia, as one of the parameters. The parameters M and H_0 are degenerate when analyzing SNe alone. However, in this analysis, we are using the full Pantheon+SH0ES dataset [14], which includes the SH0ES Cepheid host distance anchors [15] in the likelihood that facilitates constraints on both M and H_0.

Here, we use χ^2 analysis and combined statistical and systematic covariance matrices ($C_{\mathrm{stat+syst}} = C_{\mathrm{stat}} + C_{\mathrm{syst}}$) to constrain the backreaction model. We follow the formalism of [14] where cosmological parameters are constrained by minimizing a χ^2 likelihood. We incorporate SH0ES Cepheid host galaxy distance measurements into this analysis, resulting in the following supernova distance residuals:

$$\Delta \mathbf{D_i} = \begin{cases} \mu_i - \mu_i^{\mathrm{Cepheid}} & i \in \text{Cepheid hosts} \\ \mu_i - \mu_{\mathrm{model}}(z_i) & \text{otherwise,} \end{cases}$$

where μ_i^{Cepheid} is the Cepheid-calibrated host-galaxy distance provided by SH0ES. The model distances are defined as

$$\mu_{\mathrm{model}}(z_i) = 5\log(d_L(z_i)/10pc). \tag{42}$$

For the backreaction model, d_L can be calculated using the covariant scheme and standard cosmological distance relations relating angular diameter distance, D_A, to luminosity distance, d_L, as mentioned before.

In this analysis, we include the covariance matrix of Pantheon+SH0ES to calculate the likelihood

$$-2\ln(\mathcal{L}) = \chi^2 = \Delta\mathbf{D}^T (C^{\mathrm{SN}}_{\mathrm{stat+syst}} + C^{\mathrm{Cepheid}}_{\mathrm{stat+syst}})^{-1}\Delta\mathbf{D}, \tag{43}$$

where $C^{\mathrm{SN}}_{\mathrm{stat+syst}}$ denotes the SN covariance with statistical and systematic uncertainties.

In this analysis, the resulting posterior distributions of different parameters Fig. 6 are obtained using the MCMC iteration method using the MCMCSTAT package [92,93]. We use a total of 6×10^4 number of events spread across six runs with the adaptation interval of 1000 for a single run, within the parameter range given in Table I.

TABLE I. Parameter prior ranges used in the analysis.

Parameter	Range
μ_u	[0.01, 0.49]
σ_u	[0.01, 0.09]
μ_o	[0.51, 0.99]
σ_o	[0.01, 0.09]
h	[0.65, 0.80]
M	[−18, −20]

The topmost plots of each column of Fig. 6 represent the marginalized posterior distribution for the parameters μ_u, σ_u, μ_o, σ_o, h, and M, respectively, obtained by marginalizing the other parameters, while the other plots of Fig. 6 show the contour representation of the posterior distribution in different sets of two-parameter space. The darker and lighter regions denote the 1σ and 2σ confidence intervals in these contour plots. The diagonal panels display the 1-D histograms of the posterior distributions for each backreaction model parameter, obtained by marginalizing over the other parameters. The off-diagonal panels display 2D projections of the posterior probability distributions for each parameter pair, along with parameter correlations and contours. The optimum values in the plot are reported with 68% confidence limits.

Table II shows the 68% (1σ) and 95% (2σ) confidence limits for the backreaction model parameters obtained from marginalized posterior distributions from the MCMC analysis. We have 60,000 values for the backreaction model parameters from the MCMC chains. We calculated the value of τ_{reion} for the tanh reionization model for these 60, 000 sets of the backreaction model parameters' values using Eqs. (33) and (36) (see Sec. II B). We used the complete range of $z_{\mathrm{reion}} = 7.68 \pm 0.79$ for this analysis. We then used these calculated values of τ_{reion} with the MCMC chains to convert this quantity into a derived parameter. This operation helps us in analyzing the correlation between the backreaction

TABLE II. Backreaction model parameters showing 68% (1σ) and 95% (2σ) confidence limits obtained using Pantheon+SH0ES data.

Parameter	68% limits	95% limits
μ_u	$0.01308^{+0.00012}_{-0.0031}$	$0.0131^{+0.0042}_{-0.0036}$
σ_u	$0.01256^{+0.00053}_{-0.0026}$	$0.0126^{+0.0046}_{-0.0031}$
μ_o	$0.654^{+0.037}_{-0.13}$	$0.65^{+0.26}_{-0.16}$
σ_o	$0.052^{+0.030}_{-0.020}$	$0.052^{+0.037}_{-0.039}$
h	$0.7146^{+0.0089}_{-0.011}$	0.715 ± 0.023
M	$-19.132^{+0.027}_{-0.034}$	-19.132 ± 0.070

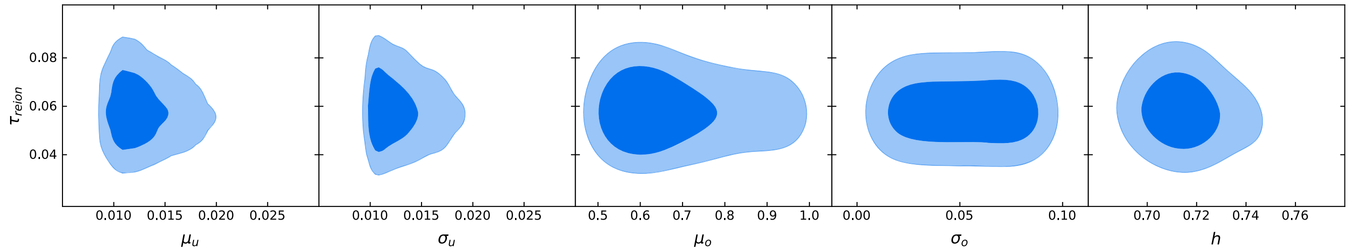

FIG. 7. Contour plots showing the correlation between the backreaction model parameters and derived parameter $\tau_{\rm reion}$.

model parameters and $\tau_{\rm reion}$ in Fig. 7. A negative correlation between $\tau_{\rm reion}$ and μ_u can be seen from Fig. 2. Increasing the value of μ_u results in a decrease in the value of $\tau_{\rm reion}$. This negative correlation is not visible in Fig. 7 as the range of μ_u constrained by the observational dataset is very narrow; hence, no correlation is visible.

The parameter μ_u represents the mean of the symmetric Gaussian distribution used to assign the deceleration parameter across the n underdense subregions. This mean serves both as the central value and the expectation value of the distribution. Consequently, the subregion(s) whose deceleration parameter lies closest to the mean value will possess the largest volume fraction and therefore contribute most significantly to volume-weighted averages over the underdense subregions.

After carrying out the MCMC analysis, we obtain a best-fit value for this parameter. The best-fit value of μ_u identifies the deceleration parameter around which the volume fraction of the underdense subregions is most strongly concentrated. Because the analysis yields a small value of $\mu_u = 0.01308$, it indicates that the MCMC procedure favors underdense regions whose local expansion histories are characterized by relatively small deceleration parameters, implying weaker deceleration and consequently a more rapidly evolving local scale factor than regions with larger $q_{ui,0}$. The best-fit value lies close to the lower end of the allowed interval, indicating a preference for underdense subregions with very weak deceleration.

The parameter σ_u denotes the standard deviation of the Gaussian distribution. A smaller $\sigma_u = 0.01256$ obtained from the MCMC analysis indicates that the distribution of the deceleration parameter among the underdense subregions is narrow and sharply peaked, implying that their local expansion histories exhibit only a small variation with only a small dispersion around the mean value.

Analogous reasoning applies to μ_o and σ_o for the Gaussian distribution that characterizes the spread of the deceleration parameter across the different overdense subregions. In particular, the best-fit value of $\mu_o = 0.654$ indicates that the volume fraction of the overdense subregions is concentrated around comparatively larger deceleration parameters, consistent with the expectation that overdense regions undergo stronger gravitational deceleration than underdense regions, while $\sigma_o = 0.052$ quantifies the spread in their local expansion histories.

Table III shows the 68% (1σ) and 95% (2σ) confidence limits for $\tau_{\rm reion}$ for four cases. The calculation of $\tau_{\rm reion}$ requires both the model of reionization and the cosmological model (see Sec. II B). The first case (i) is the direct calculation of $\tau_{\rm reion}$ from the Planck PR3 dataset for the base-ΛCDM model using the TT, TE, EE + lowE spectra reported by [1]. The remaining three cases (ii)–(iv) have been evaluated by us in this analysis. The second case is also for the Planck PR3 dataset (used here to constrain H_0), but this time using the tanh model of reionization and the ΛCDM cosmological model. The third and fourth cases employ the Pantheon+SH0ES dataset to constrain H_0, in combination with the tanh parametrization of reionization, within the frameworks of the ΛCDM and backreaction cosmological models, respectively. The last three cases

TABLE III. Optical depth to reionization measurements showing 68% (1σ) and 95% (2σ) confidence limits for $\tau_{\rm reion}$ (i) from Planck PR3 TT, TE, EE + lowE (reported in [1]); (ii) from tanh +ΛCDM model, calculated with H_0 constrained by Planck PR3 dataset; (iii) from tanh +ΛCDM model calculated with H_0 constrained by Pantheon +SH0ES dataset and (iv) from tanh +backreaction model calculated with H_0 constrained by Pantheon+SH0ES dataset. The distributions for the bottom three calculated cases are shown in Fig. 8.

$\tau_{\rm reion}$ Measurements				
S.No.	Dataset	Method	68% limits	95% limits
(i)	Planck PR3	TT, TE, EE + lowE	$0.0544^{+0.0070}_{-0.0081}$	$0.054^{+0.017}_{-0.015}$
(ii)	Planck PR3	tanh+ΛCDM	$0.0535^{+0.0079}_{-0.0076}$	$0.054^{+0.017}_{-0.015}$
(iii)	Pantheon+SH0ES	tanh+ΛCDM	$0.0476^{+0.0069}_{-0.0065}$	$0.048^{+0.013}_{-0.015}$
(iv)	Pantheon+SH0ES	tanh+backreaction	$0.0581^{+0.0105}_{-0.0096}$	$0.058^{+0.022}_{-0.019}$

have been plotted in the upper portion of Fig. 8. In the lower panel of Fig. 8, we display previously reported $\tau_{\rm reion}$ values from several observational datasets and studies, together with the $\tau_{\rm reion}$ values obtained in our own analysis.

The values listed for the first two cases in Table III are derived from the same dataset and assume the same cosmological model; only the methods used to obtain them differ. Consequently, they are expected to be equivalent, which is indeed what we observe. For the Pantheon+SH0ES dataset, the backreaction model yields a value of $\tau_{\rm reion}$ that better aligns with the Planck PR3 results than the corresponding value from the ΛCDM model.

Table IV shows the 68% (1σ) and 95% (2σ) confidence limits for H_0 for three cases. The first case (i) is reported in [1] for the Planck PR3 dataset and the ΛCDM cosmological model, where H_0 is calculated using the TT, TE, EE + lowE method. (ii) is reported in [14] for ΛCDM model using Pantheon+SH0ES dataset. (iii) is calculated here in this study for our backreaction model and Pantheon+SH0ES dataset. These quantities were then plotted in Fig. 9.

In Fig. 9, the tension between the H_0 estimates derived from the Planck PR3 data and the Pantheon+SH0ES data within the ΛCDM framework is illustrated. For the Pantheon+SH0ES dataset, the H_0 distribution inferred in

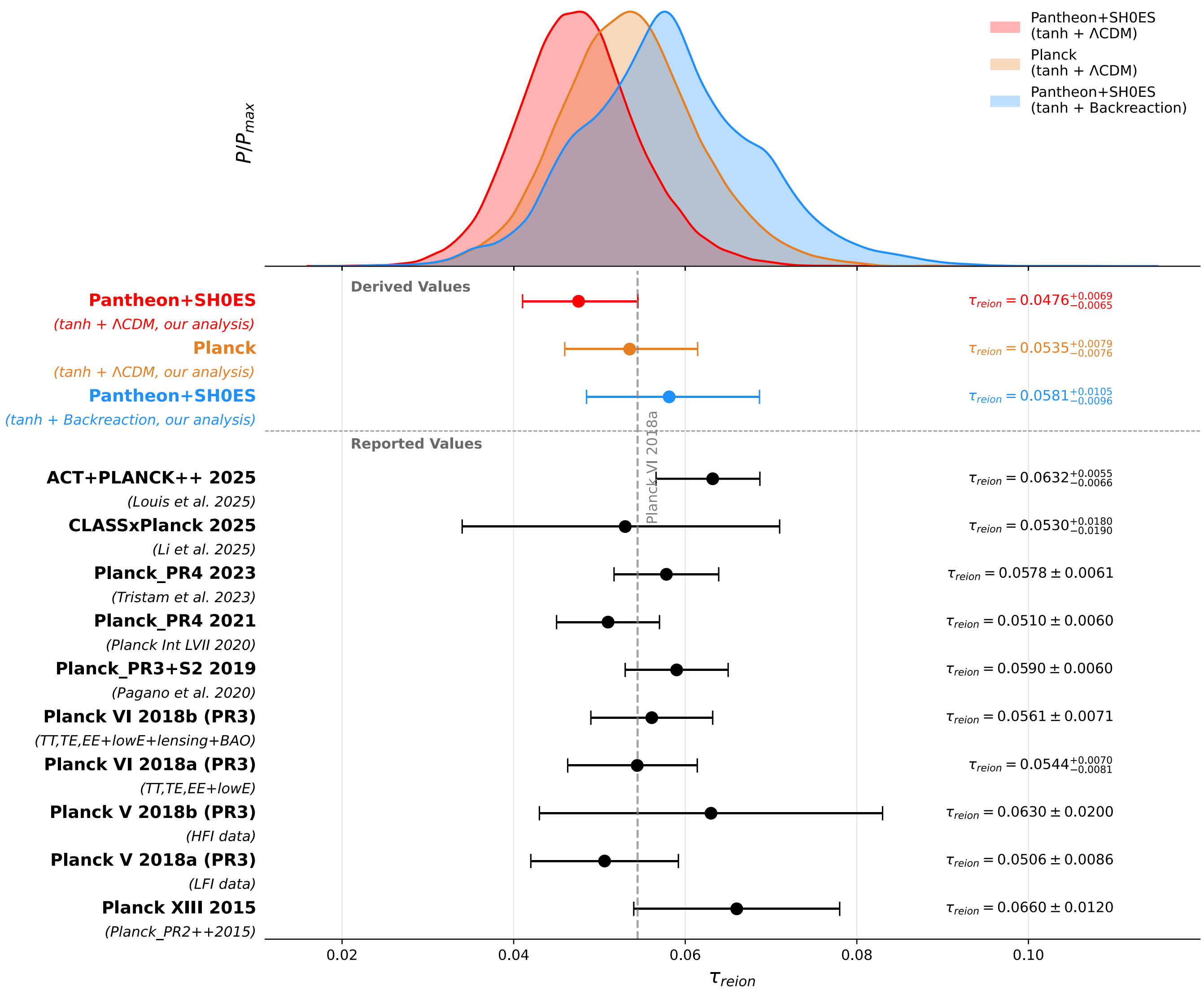

FIG. 8. The upper panel displays the distributions of $\tau_{\rm reion}$ for the tanh reionization model, shown for both the ΛCDM cosmology and the backreaction model. For the ΛCDM case, two distributions are presented: one with H_0 constrained using the Pantheon+SH0ES dataset, and the other with H_0 constrained by the Planck dataset. The backreaction model results are shown for parameters constrained by the Pantheon+SH0ES dataset. In all cases, the full allowed range of $z_{\rm re}$ has been taken into account. 68% confidence intervals of these distributions have been shown in the lower panel. The lower panel also summarizes the ranges of $\tau_{\rm reion}$ along with their 68% confidence interval, reported in various studies based on different datasets within the context of the ΛCDM model. the vertical dashed gray line is for our fiducial reference value of $\tau_{\rm reion}$ from Planck VI 2018a (PR3).

TABLE IV. Hubble constant (H_0) measurements with 68% (1σ) and 95% (2σ) confidence limits. All values in km/s/Mpc. (i) is the reported value from [1]. (ii) is reported in [14]. (iii) is calculated here in this study.

H_0 Measurements				
S.No.	Dataset	Cosmological model	68% limits	95% limits
(i)	Planck PR3 (TT, TE, EE + lowE)	ΛCDM	67.27 ± 0.60	67.3 ± 1.2
(ii)	Pantheon+SH0ES	ΛCDM	$73.45^{+1.04}_{-1.01}$	$73.45^{+2.08}_{-1.99}$
(iii)	Pantheon+SH0ES	Backreaction	$71.46^{+0.89}_{-1.1}$	71.5 ± 2.3

the backreaction framework shows significantly reduced tension with the Planck PR3 value, compared to the corresponding estimate derived within the standard cosmological model.

In summary, our methodology proceeds as follows. We first constrain the backreaction model parameters, including h and M, using the low-redshift Pantheon+SH0ES dataset. With these best-fit parameter values, we then compute $\tau_{\rm reion}$ within the framework of the tanh parametrization of reionization. This yields the corresponding prediction for $\tau_{\rm reion}$ in the combined context of the tanh reionization model and the backreaction cosmology.

For comparison, we also evaluate $\tau_{\rm reion}$ for the tanh reionization model within the ΛCDM framework, considering two cases: one in which H_0 is constrained by the Pantheon+SH0ES dataset and another in which it is constrained by the Planck PR3 dataset. These results are shown in Fig. 8 alongside the value of $\tau_{\rm reion}$ reported by Planck VI 2018 (PR3), which depends only weakly on the underlying cosmological model, as well as with estimates from other works that use different observational datasets. We find that the central value of $\tau_{\rm reion}$ inferred from the backreaction model parameters constrained by the Pantheon+SH0ES dataset agrees more closely with the values reported in numerous other studies using a variety of datasets (bottom half of Fig. 8) than does the corresponding ΛCDM-based estimate of $\tau_{\rm reion}$ obtained from the same dataset.

The value of H_0 for the backreaction model (from h in Fig. 6) that we obtain is within 2σ agreement with the value obtained by [14] for the ΛCDM model using the same Pantheon+SH0ES dataset in Fig. 9. The value of H_0 obtained from the Pantheon+SH0ES dataset is not completely independent of the cosmological model, although the dependence on the cosmological model is very minimal. We also

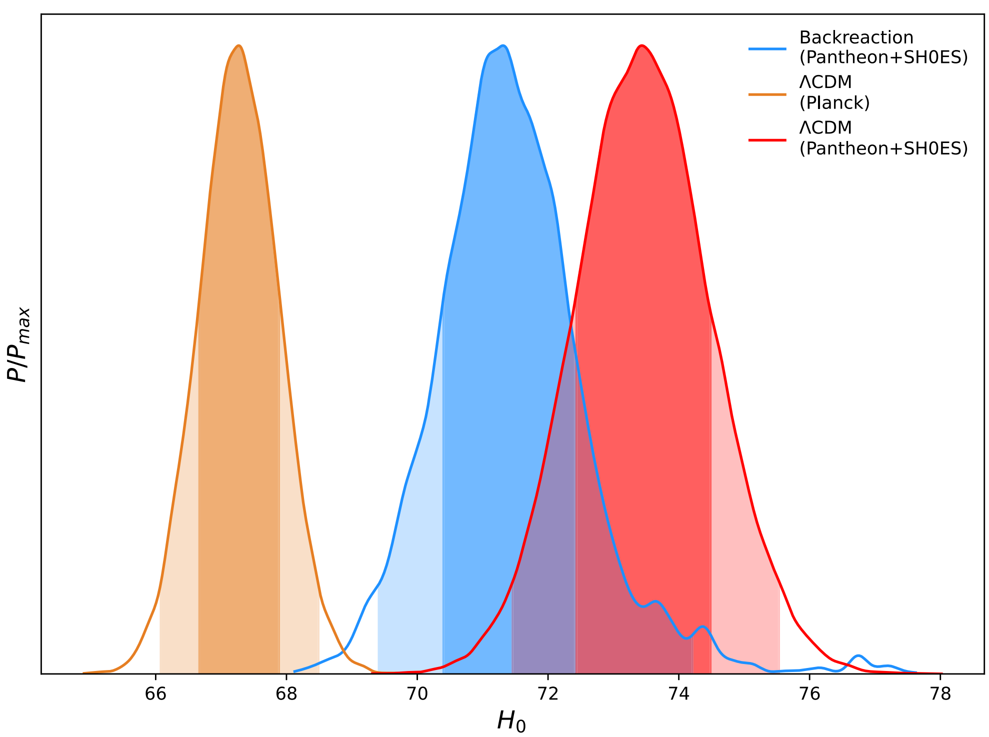

FIG. 9. This figure shows the distribution of H_0 obtained from Planck TT, TE, EE + lowE dataset (obtained by incorporating the ΛCDM model) [1], and for the Pantheon+SH0ES dataset using ΛCDM model and the backreaction model along with their 68% and 95% confidence intervals in different shades.

consider the value of H_0 for the Planck PR3 dataset for the ΛCDM cosmological model. This value is cosmological model dependent. The same figure shows that H_0 for the backreaction model from the Pantheon+SH0ES dataset is closer to that of the ΛCDM model from the Planck PR3 dataset, implying that the Hubble tension in this case is somewhat alleviated.

V. CONCLUSIONS

Recent observations indicate that the Universe contains an inhomogeneous matter distribution at considerably large scales [16,22,23]. The effects of these inhomogeneities on various cosmological phenomena warrant scrutiny. In the present study, we explore the optical depth to reionization and the associated Hubble tension under the impact of backreaction from matter inhomogeneities.

In this analysis, we use the widely used Buchert formalism [34,35] of averaging over inhomogeneities to evaluate the backreaction effect. The Buchert framework facilitates the relation of theoretically evaluated quantities with observables such as redshift and angular diameter distance [44,45,64–66]. Within this framework, we construct a backreaction model of multiple subregions with a Gaussian parameter distribution to mimic the Universe containing multiple voids and structures at the present epoch. We employ the covariant scheme to relate the theoretically evaluated parameters from the backreaction model to observational quantities.

Using this backreaction framework, we compute the reionization optical depth, $\tau_{\rm reion}$, for a particular reionization scenario, the tanh reionization model, considering both the standard ΛCDM cosmology and the backreaction cosmological model. The backreaction model we employ modifies the Hubble evolution, making it desirable to constrain its parameters using observational results. To correlate the backreaction model with observation data, we obtain the marginalized posterior densities for each model parameter through MCMC simulations using Pantheon+SH0ES supernova Ia data [2,14].

The MCMC analysis results in the dimensionless Hubble constant, one of the backreaction model parameters, $h = 0.7146^{+0.0089}_{-0.011}$, corresponding to a 68% (1σ) confidence interval. We next calculate $\tau_{\rm reion}$ by treating this parameter as a derived parameter in the MCMC analysis. We then compare the obtained values with $\tau_{\rm reion}$ from the Planck PR3 dataset. We also calculate $\tau_{\rm reion}$ for the ΛCDM and the tanh reionization model using two datasets: Pantheon+SH0ES and Planck PR3.

The analysis carried out in this study shows that the Planck results, $\tau_{\rm reion} = 0.0544^{+0.0070}_{-0.0081}$ and $z_{\rm reion} = 7.68 \pm 0.79$, are compatible within one to two sigma in the backreaction model. In particular, these values are achievable within the 68% (1σ) confidence interval for $h = 0.7146^{+0.0089}_{-0.011}$, as constrained by the Pantheon+SH0ES dataset. Furthermore, the analysis indicates a reduction in the Hubble tension. Notably, this result is obtained without invoking exotic physics or nonstandard models of dark matter and dark energy. In contrast, several previous studies have explored such extensions or modifications in attempts to address the Hubble tension [10,94–98].

Before concluding, it may be noted that in the present study, we have relied exclusively on Pantheon+SH0ES data to place constraints on our backreaction model. Incorporating additional datasets, such as DESI [99], BAO [100], H0LiCOW [101], and ACT [102], could yield significantly tighter bounds on the model parameters. Though a comprehensive analysis incorporating all available cosmological datasets would provide the most rigorous test of the backreaction model, we focus exclusively on supernova data in this work. The results obtained herein motivate extending our analysis to include a larger suite of cosmological observations in future work.

ACKNOWLEDGMENTS

S. S. P. and S. M. would like to thank the Council of Scientific and Industrial Research (CSIR), Govt of India, for funding through the CSIR-SRF-NET fellowship. The author R. acknowledges financial support from Grant No. PID2024-158938NB-I00, funded by MICIU/AEI/10.13039/501100011033 and by “ERDF/EU–A way of making Europe,” as well as from Project No. SA097P24, funded by the Junta de Castilla y León. R. also acknowledges support from “Theoretical Astroparticle Physics” (TAsP) iniziativa specifica of INFN, where part of this work was carried out. R. further acknowledges support from the S. N. Bose National Centre for Basic Sciences for her visit, where part of this work has been done. We also acknowledge the use of the HPC facility Pegasus at IUCAA, Pune, India.

DATA AVAILABILITY

There are no publicly available research data or software supporting this manuscript. Requests for further information or data should be sent to the authors.

APPENDIX: OUR MULTIDOMAIN MODEL

Our multidomain model consists of several subdomains, including both overdense and underdense regions. The underdense subdomains correspond to negatively curved FLRW regions, while the overdense subdomains correspond to positively curved FLRW regions having densities exceeding those of the underdense regions. In both cases, the subregions are modeled as dust. Now, the scale factor for these overdense and underdense subdomains as functions of cosmic time t is given by Eqs. (16)–(19), respectively.

The densities of underdense subregions is given by [82]

$$\rho_{u_i} = \frac{\rho_{u_{i,0}}}{a_{u_i}^3}, \tag{A1}$$

where $\rho_{u_{i,0}}$ is the density at present time t_0, which is given by

$$\frac{\rho_{u_{i,0}}}{\rho_{u_{i,c}}} = q_{u_{i,0}}; \quad \text{where } \rho_{u_{i,c}} = \frac{3H_{u_i,0}^2}{8\pi G}, \tag{A2}$$

where $\rho_{u_{i,c}}$ is the critical density and $H_{u_i,0}$ is the value of present time Hubble parameter for the ith underdense subregion.

Densities for the overdense subregions can also be defined similarly

$$\rho_{o_i} = \frac{\rho_{o_{i,0}}}{a_{o_i}^3}, \tag{A3}$$

where $\rho_{o_{i,0}}$ is the density at present time t_0, which is given by

$$\frac{\rho_{o_{i,0}}}{\rho_{o_{i,c}}} = q_{o_{i,0}}; \quad \text{where } \rho_{o_{i,c}} = \frac{3H_{o_i,0}^2}{8\pi G}, \tag{A4}$$

where $\rho_{o_{i,c}}$ is the critical density and $H_{o_i,0}$ is the value of present time Hubble parameter for the ith overdense subregion.

Choosing our parameters in the range $0 < q_{u_{i,0}} < 0.5$ and $1/2 < q_{o_{i,0}} < 1$, it follows from Eqs. (A2) and (A4) that the densities of underdense subdomains remain always less than the densities of overdense subdomains.

The combined density for all overdense subregions (ρ_o) is given by

$$\lambda_o \rho_o = \sum_i \lambda_{o_i} \rho_{o_i} \Rightarrow \rho_o = \frac{\sum_i \lambda_{o_i} \rho_{o_i}}{\sum_i \lambda_{o_i}}, \tag{A5}$$

where λ_{o_i} are defined in [Eq. (23)] and λ_o is the total volume fraction of the overdense subregions. Similarly,

$$\lambda_u \rho_u = \sum_i \lambda_{u_i} \rho_{u_i} \Rightarrow \rho_u = \frac{\sum_i \lambda_{u_i} \rho_{u_i}}{\sum_i \lambda_{u_i}}, \tag{A6}$$

where λ_{u_i} are defined in [Eq. (26)] and λ_u is the total volume fraction of the underdense subregions.

Also, $\langle \rho \rangle_{\mathcal{D}}$, the averaged density of the global domain is given by

$$\langle \rho \rangle_{\mathcal{D}} = \lambda_o \rho_o + \lambda_u \rho_u = \sum_i \lambda_{o_i} \rho_{o_i} + \sum_i \lambda_{u_i} \rho_{u_i}. \tag{A7}$$

The various density parameters are obtained in our analysis in the following way. From Eq. (7), we have

$$3H_{\mathcal{D}}^2 = 8\pi G \langle \rho \rangle_{\mathcal{D}} - \frac{1}{2} \langle \mathcal{R} \rangle_{\mathcal{D}} - \frac{1}{2} \mathcal{Q}_{\mathcal{D}.} \tag{A8}$$

Dividing by $3H_{\mathcal{D}}^2$ throughout, we get

$$1 = \Omega_m^{\mathcal{D}} + \Omega_{\mathcal{R}}^{\mathcal{D}} + \Omega_{\mathcal{Q}}^{\mathcal{D}}, \tag{A9}$$

where,

$$\Omega_m^{\mathcal{D}} = \frac{8\pi G \langle \rho \rangle_{\mathcal{D}}}{3H_{\mathcal{D}}^2}; \qquad \Omega_{\mathcal{R}}^{\mathcal{D}} = -\frac{\langle \mathcal{R} \rangle_{\mathcal{D}}}{6H_{\mathcal{D}}^2}; \qquad \Omega_{\mathcal{Q}}^{\mathcal{D}} = -\frac{\mathcal{Q}_{\mathcal{D}}}{6H_{\mathcal{D}}^2}. \tag{A10}$$

From Eq. (27), we can calculate $\mathcal{Q}_{\mathcal{D}}$ for our model and then from Eq. (A10), $\Omega_{\mathcal{Q}}^{\mathcal{D}}$ can be calculated. Then using Eqs. (A7) and (A10), $\Omega_m^{\mathcal{D}}$ can be calculated and $\Omega_{\mathcal{R}}^{\mathcal{D}}$ can be calculated from Eq. (A9). In this way, all the average density parameters can be obtained.

[1] N. Aghanim, Y. Akrami et al. (Planck Collaboration), Astron. Astrophys. **641**, A6 (2020).
[2] D. Scolnic, D. Brout, A. Carr et al., Astrophys. J. **938**, 113 (2022).
[3] N. Suzuki et al., Astrophys. J. **746**, 85 (2012).
[4] L. Perivolaropoulos and F. Skara, New Astron. Rev. **95**, 101659 (2022).
[5] A. Del Popolo and M. Le Delliou, Galaxies **5**, 17 (2017).
[6] E. Abdalla, G. F. Abellán, A. Aboubrahim et al., J. High Energy Astrophys. **34**, 49 (2022).
[7] E. Di Valentino, Universe **8**, 399 (2022).
[8] E. Di Valentino, J. L. Said, A. Riess et al., Phys. Dark Universe **49**, 101965 (2025).
[9] L. Perivolaropoulos and F. Skara, New Astron. Rev. **95**, 101659 (2022).
[10] E. Di Valentino, O. Mena, S. Pan, L. Visinelli, W. Yang, A. Melchiorri, D. F. Mota, A. G. Riess, and J. Silk, Classical Quantum Gravity **38**, 153001 (2021).
[11] J.-P. Hu and F.-Y. Wang, Universe **9**, 94 (2023).
[12] J. L. Cervantes-Cota, S. Galindo-Uribarri, and G. F. Smoot, Universe **9**, 501 (2023).
[13] L. Verde, N. Schöneberg, and H. Gil-Marín, Annu. Rev. Astron. Astrophys. **62**, 287 (2024).

[14] D. Brout, D. Scolnic, B. Popovic *et al.*, Astrophys. J. **938**, 110 (2022).
[15] A. G. Riess, W. Yuan, L. M. Macri *et al.*, Astrophys. J. Lett. **934**, L7 (2022).
[16] F. S. Labini, N. L. Vasilyev, L. Pietronero, and Y. V. Baryshev, Europhys. Lett. **86**, 49001 (2009).
[17] T. Buchert, A. A. Coley, H. Kleinert *et al.*, Int. J. Mod. Phys. D **25**, 1630007 (2016).
[18] F. Sylos Labini and L. Pietronero, J. Stat. Mech. (2010) P11029.
[19] F. S. Labini, Classical Quantum Gravity **28**, 164003 (2011).
[20] A. O. Verevkin, Y. L. Bukhmastova, and Y. V. Baryshev, Astronomy Reports **55**, 324 (2011).
[21] P. Kumar Aluri, P. Cea, P. Chingangbam *et al.*, Classical Quantum Gravity **40**, 094001 (2023).
[22] A. Wiegand, T. Buchert, and M. Ostermann, Mon. Not. R. Astron. Soc. **443**, 241 (2014).
[23] A. M. Lopez, R. G. Clowes, and G. M. Williger, Mon. Not. R. Astron. Soc. **516**, 1557 (2022).
[24] A. M. Lopez and R. G. Clowes, arXiv:2504.14940.
[25] T. Sawala, M. Teeriaho, C. S. Frenk *et al.*, arXiv:2502.03515.
[26] T. Sawala and M. Teeriaho, **8**, 10.33232/001c.145931 (2025).
[27] A. Wiegand and T. Buchert, Phys. Rev. D **82**, 023523 (2010).
[28] S. Räsänen, J. Cosmol. Astropart. Phys. 11 (2006) 003.
[29] G. F. R. Ellis, Relativistic cosmology: Its nature, aims and problems, in *General Relativity and Gravitation: Invited Papers and Discussion Reports of the 10th International Conference on General Relativity and Gravitation, Padua, July 3–8, 1983*, edited by B. Bertotti, F. de Felice, and A. Pascolini (Springer Netherlands, Dordrecht, 1984), pp. 215–288.
[30] T. Futamase, Phys. Rev. Lett. **61**, 2175 (1988).
[31] R. M. Zalaletdinov, Gen. Relativ. Gravit. **24**, 1015 (1992).
[32] R. M. Zalaletdinov, Gen. Relativ. Gravit. **25**, 673 (1993).
[33] M. Gasperini, G. Marozzi, F. Nugier, and G. Veneziano, J. Cosmol. Astropart. Phys. 07 (2011) 008.
[34] T. Buchert, Gen. Relativ. Gravit. **32**, 105 (2000).
[35] T. Buchert, Gen. Relativ. Gravit. **33**, 1381 (2001).
[36] A. A. Coley, N. Pelavas, and R. M. Zalaletdinov, Phys. Rev. Lett. **95**, 151102 (2005).
[37] M. Korzyński, Classical Quantum Gravity **27**, 105015 (2010).
[38] T. Clifton, K. Rosquist, and R. Tavakol, Phys. Rev. D **86**, 043506 (2012).
[39] H. Skarke, Phys. Rev. D **89**, 043506 (2014).
[40] T. Buchert, M. Carfora, G. F. R. Ellis *et al.*, Classical Quantum Gravity **32**, 215021 (2015).
[41] S. Räsänen, J. Cosmol. Astropart. Phys. 02 (2004) 003.
[42] D. L. Wiltshire, Dark energy without dark energy, in *Dark Matter in Astroparticle and Particle Physics* (World Scientific, Singapore, 2008), pp. 565–596.
[43] E. W. Kolb, S. Matarrese, and A. Riotto, New J. Phys. **8**, 322 (2006).
[44] S. Koksbang, J. Cosmol. Astropart. Phys. 10 (2019) 036.
[45] S. M. Koksbang, Mon. Not. R. Astron. Soc.: Lett. **498**, L135 (2020).
[46] S. M. Koksbang, Phys. Rev. Lett. **126**, 231101 (2021).
[47] S. Räsänen, J. Cosmol. Astropart. Phys. 04 (2008) 026.
[48] N. Bose and A. S. Majumdar, Mon. Not. R. Astron. Soc.: Lett. **418**, L45 (2011).
[49] N. Bose and A. S. Majumdar, Gen. Relativ. Gravit. **45**, 1971 (2013).
[50] A. Ali and A. Majumdar, J. Cosmol. Astropart. Phys. 01 (2017) 054.
[51] S. S. Pandey, A. Sarkar, A. Ali, and A. Majumdar, J. Cosmol. Astropart. Phys. 06 (2022) 021.
[52] S. S. Pandey, A. Sarkar, A. Ali, and A. S. Majumdar, Eur. Phys. J. C **83**, 435 (2023).
[53] S. Koksbang and S. Hannestad, J. Cosmol. Astropart. Phys. 01 (2016) 009.
[54] S. M. Koksbang, Phys. Rev. D **106**, 063514 (2022).
[55] S. M. Koksbang, Phys. Rev. D **107**, 103522 (2023).
[56] S. M. Koksbang, Phys. Rev. Lett. **130**, 201003 (2023).
[57] S. M. Koksbang, Phys. Rev. D **107**, 103522 (2023).
[58] S. S. Pandey, A. Halder, and A. S. Majumdar, Phys. Rev. D **110**, 043531 (2024).
[59] S. Mukherjee, S. S. Pandey, and A. S. Majumdar, Phys. Rev. D **112**, 063520 (2025).
[60] K. Lodha, R. Calderon, W. L. Matthewson *et al.*, Phys. Rev. D **112**, 083511 (2025).
[61] J. Son, Y.-W. Lee, C. Chung, S. Park, and H. Cho, Mon. Not. R. Astron. Soc. **544**, 975 (2025).
[62] A. Halder, S. S. Pandey, and A. Majumdar, J. Cosmol. Astropart. Phys. 08 (2023) 064.
[63] L. Giani, R. von Marttens, and R. Camilleri, Phys. Rev. Lett. **135**, 071004 (2025).
[64] S. Räsänen, J. Cosmol. Astropart. Phys. 02 (2009) 011.
[65] S. Räsänen, J. Cosmol. Astropart. Phys. 03 (2010) 018.
[66] S. M. Koksbang, Classical Quantum Gravity **36**, 185004 (2019).
[67] S. Koksbang, J. Cosmol. Astropart. Phys. 11 (2020) 061.
[68] M. Kasai and T. Futamase, Prog. Theor. Exp. Phys. **2019**, 073E01 (2019).
[69] H. J. Macpherson, P. D. Lasky, and D. J. Price, Astrophys. J. Lett. **865**, L4 (2018).
[70] T. Miura and T. Tanaka, J. Cosmol. Astropart. Phys. 05 (2024) 126.
[71] M. San Martín and C. Rubio, Ann. Phys. (Amsterdam) **458**, 169444 (2023).
[72] K. Bolejko, Phys. Rev. D **97**, 103529 (2018).
[73] A. Heinesen and T. Buchert, Classical Quantum Gravity **37**, 164001 (2020).
[74] I. Ben-Dayan, R. Durrer, G. Marozzi, and D. J. Schwarz, Phys. Rev. Lett. **112**, 221301 (2014).
[75] L. M. Griffiths, D. Barbosa, and A. R. Liddle, Mon. Not. R. Astron. Soc. **308**, 854 (1999).
[76] K. Wolz, N. Krachmalnicoff, and L. Pagano, Astron. Astrophys. **676**, A30 (2023).
[77] L. Pagano, J.-M. Delouis, S. Mottet, J.-L. Puget, and L. Vibert, Astron. Astrophys. **635**, A99 (2020).
[78] R. de Belsunce, S. Gratton, W. Coulton, and G. Efstathiou, Mon. Not. R. Astron. Soc. **507**, 1072 (2021).

[79] T. Jhaveri, T. Karwal, and W. Hu, Phys. Rev. D **112**, 043541 (2025).
[80] Z. Huang, Mon. Not. R. Astron. Soc. **544**, 2193 (2025).
[81] T. Buchert and S. Räsänen, Annu. Rev. Nucl. Part. Sci. **62**, 57 (2012).
[82] S. Weinberg, *Gravitation and Cosmology: Principles and Applications of the General Theory of Relativity* (John Wiley and Sons, New York, 1972).
[83] D. N. Schramm and M. S. Turner, Rev. Mod. Phys. **70**, 303 (1998).
[84] A. Lewis, Phys. Rev. D **78**, 023002 (2008).
[85] Planck Collaboration, P. A. R. Ade, N. Aghanim *et al.*, Astron. Astrophys. **594**, A13 (2016).
[86] Planck Collaboration, N. Aghanim, Y. Akrami *et al.*, Astron. Astrophys. **641**, A5 (2020).
[87] Planck Collaboration, Y. Akrami, K. J. Andersen *et al.*, Astron. Astrophys. **643**, A42 (2020).
[88] M. Tristram, A. J. Banday, M. Douspis *et al.*, Astron. Astrophys. **682**, A37 (2024).
[89] Y. Li, J. R. Eimer, J. W. Appel *et al.*, Astrophys. J. **986**, 111 (2025).
[90] T. Louis, A. La Posta, Z. Atkins *et al.*, J. Cosmol. Astropart. Phys. 11 (2025) 062.
[91] R. Tripp, Astron. Astrophys. **331**, 815 (1998).
[92] H. Haario, M. Laine, A. Mira, and E. Saksman, Stat. Comput. **16**, 339 (2006).
[93] H. Haario, E. Saksman, and J. Tamminen, Bernoulli **7**, 223 (2001).
[94] T. Karwal and M. Kamionkowski, Phys. Rev. D **94**, 103523 (2016).
[95] G.-B. Zhao, M. Raveri, L. Pogosian *et al.*, Nat. Astron. **1**, 627 (2017).
[96] W. Yang, S. Pan, S. Vagnozzi, E. Di Valentino, D. F. Mota, and S. Capozziello, J. Cosmol. Astropart. Phys. 11 (2019) 044.
[97] S. Kumar and R. C. Nunes, Phys. Rev. D **94**, 123511 (2016).
[98] J. P. Johnson, A. Sangwan, and S. Shankaranarayanan, J. Cosmol. Astropart. Phys. 01 (2022) 024.
[99] M. Abdul Karim, J. Aguilar, S. Ahlen *et al.* (DESI Collaboration), Phys. Rev. D **112**, 083515 (2025).
[100] K. S. Dawson, J.-P. Kneib, W. J. Percival *et al.*, Astron. J. **151**, 44 (2016).
[101] K. C. Wong, S. H. Suyu, G. C.-F. Chen *et al.*, Mon. Not. R. Astron. Soc. **498**, 1420 (2020).
[102] M. S. Madhavacheril, F. J. Qu, B. D. Sherwin *et al.*, Astrophys. J. **962**, 113 (2024).